DEPARTMENT OF PHYSICS
UNIVERSITY OF JYVÄSKYLÄ
RESEARCH REPORT No. 8/2001

IN-BEAM SPECTROSCOPY OF VERY HEAVY ELEMENTS

BY
HARRI KANKAANPÄÄ

Academic Dissertation
for the Degree of
Doctor of Philosophy

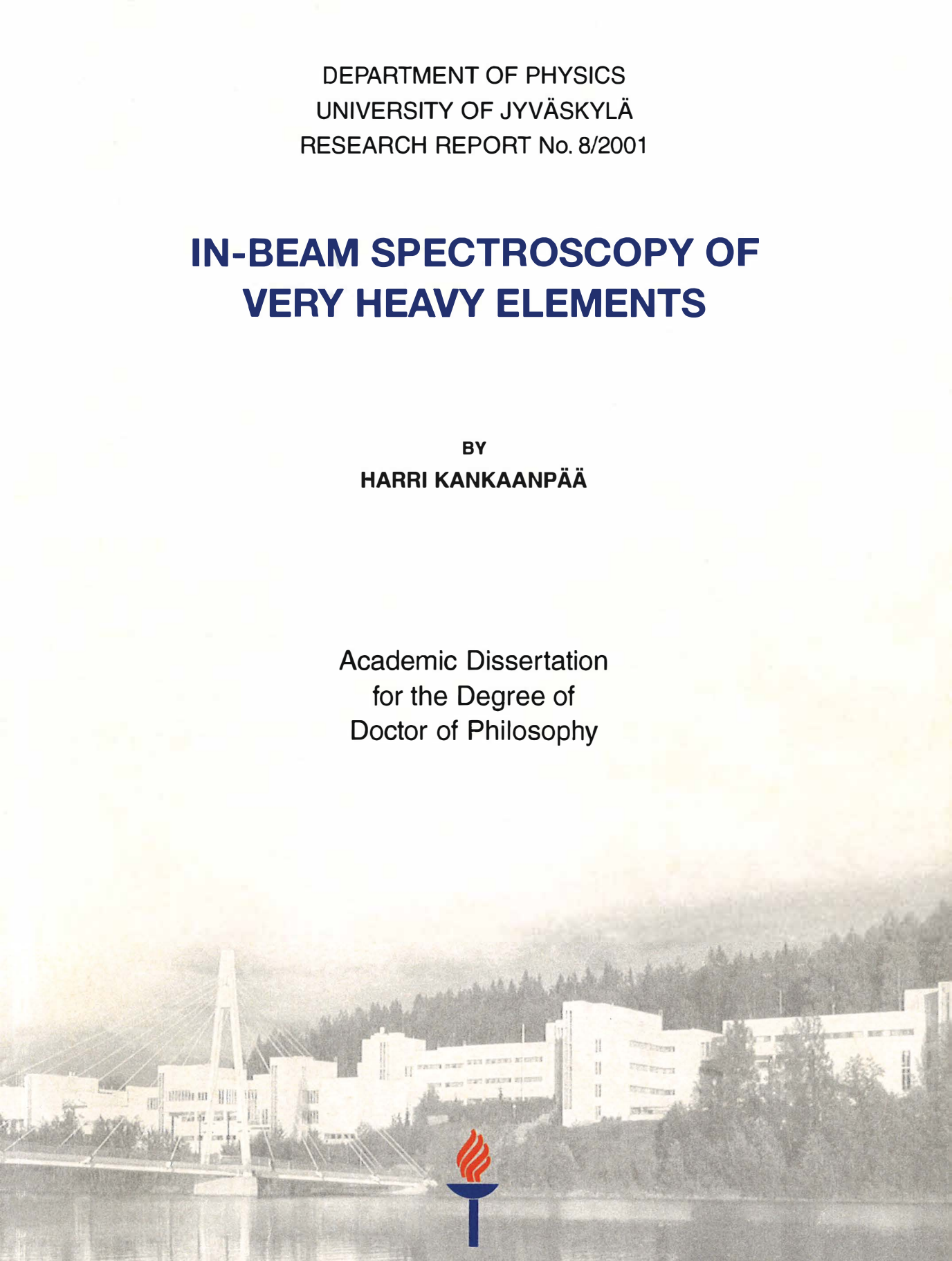

Jyväskylä, Finland
August, 2001

DEPARTMENT OF PHYSICS,
UNIVERSITY OF JYVÄSKYLÄ
RESEARCH REPORT No. 8/2001

IN-BEAM SPECTROSCOPY OF VERY HEAVY ELEMENTS

BY
HARRI KANKAANPÄÄ

Academic Dissertation
for the Degree of
Doctor of Philosophy

To be presented, by permission of the
Faculty of Mathematics and Natural Sciences
of the University of Jyväskylä,
for public examination in Auditorium FYS-1 of the
University of Jyväskylä on August 16, 2001
at 12 o'clock noon

Jyväskylä, Finland
August 2001

URN:ISBN:978-951-39-9738-0
ISBN 978-951-39-9738-0 (PDF)
ISSN 0075-465X

Jyväskylän yliopisto, 2023

ISBN 951-39-1029-6
ISSN 0075-465X

Preface

I started to work with this thesis in January 1997 at the Accelerator Laboratory of the University of Jyväskylä.

I wish to express my gratitude to my supervisor Prof. Rauno Julin for his guidance, encouragement and trust in my design skills. I am also grateful to Prof. Matti Leino for his guidance into the secrets of recoil separators and the studies of very heavy elements. I would like to thank Prof. Peter Butler for guiding me through the mysteries of electron spectroscopy. Special thanks to Dr. Paul Greenlees and Dr. Alex Keenan for their help and suggestions in writing this thesis. Thanks go also to all members in the combined conversion-electron, γ-ray and RITU group. It has been a great honour to work with such inspiring people.

The atmosphere at the Department of Physics has been exceptionally friendly. This cannot be just due to the fantastic location of the department, but due to the excellent staff and fruitful collaborations. I also would like to thank the mechanical workshop helping me with the designs.

The financial support from the University of Jyväskylä and the Graduate School of Particle and Nuclear Physics are gratefully acknowledged.

Finally, I would like to thank my family, my wife Tiina and our sons Ville and Joonas for their patience and loving during these years.

Jyväskylä, June 2001

Harri Kankaanpää

Abstract

Novel in-beam spectroscopic methods utilising the recoil-gating and recoil-decay-tagging techniques were employed for the spectroscopy of very heavy elements ^{252,253,254}No and ^{255}Lr. In-beam γ-ray spectroscopy of these nuclei is based on the use of germanium detector arrays in conjunction with the gas-filled recoil separator RITU. The major part of this work was to design the collinear SACRED electron spectrometer to be used in conjunction with RITU. For the first time it was possible to obtain recoil-gated conversion-electron spectra. The ground-state bands in the even-even ^{252,254}No nuclei were observed. Global systematics and the extrapolated energy of the lowest 2^+ state were used to deduce the deformation parameter β_2 for these nuclei. The studies of odd-A ^{253}No and ^{255}Lr nuclei indicated that the de-excitations in these nuclei mainly proceed via cascades of M1-transitions.

Contents

Introduction 1

1 Nuclear Properties **5**

1.1 Macroscopic and microscopic description of nuclei 5

1.2 Rotational quantities 7

1.3 Electromagnetic transitions in nuclei 9

1.4 Production of the heavy elements 13

2 Spectroscopic methods **15**

2.1 Recoil Separators 15

2.1.1 RITU gas-filled recoil separator 17

2.1.2 Decay spectroscopy 18

2.2 In-beam gamma-ray spectroscopy 21

2.2.1 Jurosphere-array 23

2.2.2 SARI-array . . . 25

2.3 Conversion electron spectroscopy 28

2.4 Collinear conversion electron spectrometer 31

2.4.1 Performance 37

3 Electronics and data processing **45**

3.1 Electronics for the arrays at the target area 45

3.2 RITU electronics 47

3.3 Data Acquisition 48

3.4 RDT method . . 49

4 Experimental studies of No and Lr nuclei **51**

4.1 Even-even No nuclei 52

4.1.1 Gamma-ray and electron spectroscopic studies of ^{254}No 52

4.1.2 Gamma-rays from ^{252}No 61

4.2 Odd-A ^{253}No and ^{255}Lr nuclei . 65

4.2.1 Gamma-rays from ^{255}Lr 65

4.2.2 Electron spectroscopic studies of ^{253}No 67

4.3 Discussion 70

5 Summary **73**

Appendix **75**

A Relativistic corrections for electrons and gamma-rays **75**

Bibliography **79**

Introduction

One of the most interesting fields of study in nuclear physics is to determine the limits of existence of nuclei. According to the simple liquid drop model, heavy nuclei with $Z > 100$ should be unbound against spontaneous fission. However, it is found that when shell effects are taken into account, these nuclei are bound. The Nilsson-Strutinsky shell-correction approach is widely used to calculate properties of super-heavy elements ($Z > 114$) [Ćwi 94], but the predictions strongly depend on the parametrization of the model. Structure information of the known lighter nuclei is used to constrain the model parameters. Therefore it is important to extend the structure studies of nuclei as close as possible to the region of super-heavy elements. A fascinating fact is that there is enhanced stability against fission in the region between super-heavy elements and known nuclei [Hof 99]. The stabilization is due to shell effects of deformed nuclei, the most important component of the deformation being quadrupole deformation [Möl 95]. For this reason the main decay mode of the heaviest known elements is α decay. Spectroscopy of the heaviest odd-mass nuclei would provide information about the ordering and excitation energies of single-particle states near the Fermi surface. Measurements of the lowest excited states in even-even nuclei give information about the deformation.

Production cross-sections of the super-heavy elements are on the order of 1 pb, well below the limit at which in-beam spectroscopic studies can be performed ($\sigma \approx 1$ μb). Therefore it is not (yet) possible to probe properties of excited states of the super-heavy elements by means of in-beam methods. In general, production cross-sections of the nuclei heavier than Pu are below this limit. However, exceptionally high cross-sections (≈ 1 μb) have been measured for cold fusion of doubly magic ^{48}Ca and nuclei around ^{208}Pb. These reactions produce nuclei close to ^{254}No, but the production cross-sections are still too low for in-beam measurements without special triggering methods.

Recent studies of very light Hg, Po and Pb nuclei have shown that it is possible to perform in-beam γ-ray spectroscopy for nuclei with production cross-sections on the order of a few hundred nb [Jen 00, Mui 00, Hel 99, LeC 99]. The required selectivity is achieved by using the techniques of recoil-gating and recoil-decay tagging (RDT) [Pau 95, Sim 86]. The excitation function of the heaviest elements in fusion evaporation reactions is very narrow due to the competition between fusion and fission and therefore practically only one fusion evaporation channel is open. This is an exceptional feature compared to the production of the lighter nuclei. Since only one channel is open, the recoil-gating method is sufficient to isolate the transitions of interest. Detection of these fusion evaporation residues (recoils) allows the prompt γ-rays or conversion electrons to be "tagged" in order to remove the dominant background radiation arising from fission events. Identification of the recoils is based on their magnetic rigidities, velocities, decay properties etc. Observation of the prompt γ-rays with high energy resolution is achieved with arrays of high-purity Ge-detectors which surround the target area. For the study of nuclei with production cross sections on the order of a few μb it is necessary to have a high-efficiency recoil separator and a high-efficiency Ge-detector array.

In this work, novel in-beam γ-ray and conversion-electron spectroscopic methods were used to investigate the structure of ^{252,253,254}No and ^{255}Lr by employing recoil-gating and RDT techniques. For the first time, it was possible to use in-beam conversion-electron spectroscopic methods together with recoil-gating and RDT techniques.

All of the experiments discussed in the present work were performed at the Accelerator Laboratory of the University of Jyväskylä (JYFL). The ^{48}Ca beam was produced in the ECR ion-source and accelerated by the K = 130 MeV cyclotron [Hei 95]. Joint-European projects allowed the construction of different detector arrays for various time periods. The γ-ray spectroscopic studies of ^{254}No, ^{252}No and ^{255}Lr presented in this work are reported in [Lei 99], [Her 01a] and [Gre 01], respectively. One of the major goals in this

work was to redesign an electron spectrometer for use in conjunction with the gas-filled recoil separator RITU [Lei 95] at JYFL. A technical description of this device will be published in the near future [Kan 01]. It was used for in-beam conversion electron spectroscopic studies of ^{254}No and ^{253}No reported in [But 01] and [Her 01b], respectively. The author was responsible for the development and design work in these projects. The data published in this work has been mainly analysed by the author.

Chapter 1

Nuclear Properties

1.1 Macroscopic and microscopic description of nuclei

Early studies of the properties of nuclei showed that nuclear matter has a very low compressibility and approximately constant density. Constant density means that the volume of the nucleus is proportional to the number of the nucleons ($V \propto A$), and if the shape is considered to be spherical, the nuclear radius (R) is thus proportional to $A^{1/3}$, giving

$$R = r_0 A^{1/3}, \tag{1.1}$$

where the radius r_0 is approximately 1.4 fm for nuclear matter and 1.20 - 1.45 fm for nuclear charge. Low compressibility is analogous to that for a macroscopic drop of fluid. The particle evaporation phenomenon is in analogy to molecular evaporation from the surface of the liquid drop. Fission can be thought of as splitting the drop into two smaller droplets. The binding energy of the nucleus can be described by the semi-empirical mass formula, formulated by Von Weizsäcker [Wei 35],

$$B(Z,A) = a_v A - a_s A^{\frac{2}{3}} - a_c \frac{Z^2}{A^{\frac{1}{3}}} - a_{sym} \frac{(N-Z)^2}{A} - \delta(Z,N). \tag{1.2}$$

Experimentally observed binding energies are used to fit the different parameters (a_v, a_s, a_c, a_{sym}, δ) in order to predict masses of unknown nuclei. The liquid drop model (LDM) does not contain any information about the microscopic structure of the nucleus, and therefore some discrepancies (e.g. mass difference between experimental and theoretical values) can be seen at magic numbers (N or Z = 2, 8, 20, 28, 50, 82 and N = 126). The formula does not reproduce the enhanced binding of nuclei with these neutron or proton numbers. When the LDM is applied to heavy elements ($Z > 100$), the Coulomb energy is so large that these nuclei should be unstable against spontaneous fission. However, in experimental studies it has been observed that the heaviest elements are α-emitters with half-lives $>$ 1 ms. This enhanced stability against fission is almost entirely due to shell effects. For this reason a microscopic approach is needed.

Fully analytic microscopic calculations of nuclear properties would require a solution of the many-body Schrödinger equation, where the Hamiltonian $\mathcal{H}$ is of the form

$$\mathcal{H} = \mathcal{T} + \sum_{i<j} \mathcal{V}_{ij}. \tag{1.3}$$

Here $\mathcal{T}$ is a sum of the individual kinetic energies of all the nucleons, and $\mathcal{V}_{ij}$ is the nucleon-nucleon interaction. It is impossible to solve this in general, and therefore simplifications are needed. When the nucleon-nucleon interaction is replaced with the mean field approximation, the Schrödinger equation becomes separable and can be solved as a one-particle problem.

The spherical shell model describes nucleons as independent particles moving in the effective (spherical) mean field generated by all the other nucleons. With incorporation of the strong spin-orbit interaction one obtains the shell structure with the correct magic numbers. Any single-particle state can then be presented using the quantum numbers n, j, m_j. Each j-state has $2j+1$ degenerate states. In a simple picture, the nuclear excitations can be thought

of as a single particle occupying different states.

If the nucleus has a non-spherical shape, collective excitations are possible. The general shape of the nucleus is presented as a sum of the spherical harmonics [But 96b]

$$R(\Omega) = c(\alpha)R_0\left[1 + \sum_{\lambda=2}^{\lambda_{max}} \sum_{\mu=-\lambda}^{+\lambda} \alpha_{\lambda\mu} Y^*_{\lambda\mu}(\Omega)\right], \tag{1.4}$$

where $c(\alpha)$ is introduced to keep the volume of the nucleus constant. In the case of axially symmetric shapes, the deformation parameters with $\mu \neq 0$ vanish. Large experimentally measured quadrupole moments suggest static deformation allowing collective rotation at low frequencies.

The first investigation of the effect of deformation on the single-particle orbitals was performed by S.G. Nilsson [Nil 55]. The resulting Nilsson-states are mixtures of the different j-states. This means that the spherical shell model quantum numbers are no longer good quantum numbers, but the projections Ω of j onto the symmetry axis are. Therefore the eigenstates are labelled by the asymptotic quantum numbers $[Nn_z\Lambda]\Omega^\pi$ (Nilsson orbitals). The orbitals with low Ω-values favour prolate shapes ($\beta > 0$), whereas orbitals with high Ω-values favour oblate shapes ($\beta < 0$).

1.2 Rotational quantities

Deformed nuclei can be found in the mass regions $150 < A < 190$ and $A > 220$. The lowest excited states of these nuclei are collective rotational states. The rotational energy of the quantum-mechanical rotating object is

$$E(I) = \frac{\hbar^2}{2\mathcal{J}} I(I+1), \tag{1.5}$$

where I is the angular-momentum quantum number (nuclear spin in nuclei)

and $\mathcal{J}$ the moment of inertia. The rotational frequency ω of the nucleus at a given spin I is given by the following expression

$$\hbar\omega = \frac{dE(I)}{dI}, \tag{1.6}$$

which for an E2 transition energy E_γ between the states of spin I and $I-2$ approximates to $E_\gamma/2$. For an ideal rotor, the moment of inertia $\mathcal{J}$ is constant. In general, the nuclear rotation is not that of a rigid body, but the moment of inertia is a function of the rotational frequency ω. The moment of inertia for nuclei is normally smaller than that for a rigid body, but larger than that expected for a fluid inside a rotating ellipsoidal vessel. However, moment of inertia values have been found to be exceptionally close to that of a rigid body for superdeformed nuclei.

Three types of moments of inertia are used to describe the rotational behaviour of nuclei, the static $\mathcal{J}^{(0)} = \mathcal{J}$, the kinematic $\mathcal{J}^{(1)}$ and the dynamic $\mathcal{J}^{(2)}$. The kinematic moment of inertia is given by

$$\mathcal{J}^{(1)}(I) = \left[\frac{2}{\hbar^2}\frac{dE(I)}{d(I^2)}\right]^{-1}, \tag{1.7}$$

and the dynamic moment of inertia by

$$\mathcal{J}^{(2)}(I-1) = \left[\frac{1}{\hbar^2}\frac{d^2E(I)}{dI^2}\right]^{-1}. \tag{1.8}$$

For quadrupole rotations these can be approximated as $\mathcal{J}^{(1)} \approx \hbar^2(2I-1)/E_\gamma$ and $\mathcal{J}^{(2)} \approx 4\hbar^2/\Delta E_\gamma$, where spin I stands for the initial state ($E_\gamma = E(I) - E(I-2)$).

The Variable Moment of Inertia (VMI) method was proposed by Harris [Har 65] assuming that

$$\mathcal{J}^{(1)} = \mathcal{J}_0 + \mathcal{J}_1\omega^2, \tag{1.9}$$

which introduces the Harris parameters $\mathcal{J}_0$ and $\mathcal{J}_1$. For the unknown members of the band, different assumptions of spin I need to be made in order to calculate $\mathcal{J}^{(1)}$ values for observed transitions. When these values are plotted as a function of ω^2, the curve closest to a straight line represents the correct spin assignment. This method was employed for ^{252,254}No nuclei and is discussed in sections 4.1.1 and 4.1.2.

The Harris parameters can be fitted when the correct assumption is made. Furthermore, the fitted Harris parameters can be used to extrapolate the energies of the unknown states at low spin (e.g. the energy of the first excited 2^+ state). The formula to relate the rotational frequency ω $(=\frac{E_\gamma}{2\hbar})$ and the spin value I is derived from equations 1.7 and 1.9:

$$I(\omega) = \omega[\mathcal{J}_0 + \mathcal{J}_1\omega^2] + \frac{1}{2}. \tag{1.10}$$

This equation was used to extrapolate the $2^+ \longrightarrow 0^+$ and the $4^+ \longrightarrow 2^+$ transitions in ^{252,254}No nuclei which were not observed in the γ-ray studies (see sections 4.1.1 and 4.1.2).

1.3 Electromagnetic transitions in nuclei

Properties of the excited states in nuclei provide information about the structure of the nucleus. The de-excitation of the initial state with an energy of E_i to the final state with E_f generally proceeds via the emission of a γ-ray or a conversion electron. When the de-excitation proceeds via internal conversion, the energy of the conversion electron is $E_{e^-} = E_i - E_f - B$, where B is the electron binding energy. The electrons in different atomic shells have different binding energies which splits the transition into different lines in the electron spectrum.

Conservation of the total angular momentum limits the multipolarity L of

the transition. For a rotational band in a quadrupole-deformed even-even nucleus, the lowest possible multipolarity transition is electric quadrupole E2. In odd-mass heavy nuclei, it is possible that the de-excitations mainly proceeds via M1-transitions in the case of strongly coupled bands, but via E2-transitions in the decoupled case.

The intensity ratio between emitted conversion-electrons and γ-rays is known as the total conversion coefficient α_{tot}. Total conversion coefficients [Ros 78] for E2 and M1-transitions for nuclei with $Z = 102$ in the energy range of 10 - 500 keV are plotted in Fig. 1.1. Internal conversion dominates for E2-transitions with energies below 250 keV, and for M1-transitions below 400 keV. Note that for an E2-transition, the L-conversion dominates at all transition energies above the L-binding energy, whereas for the M1-transitions the K-conversion is strongest for transition energies greater than the K-binding energy ($\sim$ 150 keV). A typical intensity ratio for K and L-conversion (K/L) of the E2-transition is $\frac{1}{20}$ to 1 in the shown energy range above 150 keV. It is interesting that an almost constant K/L ratio of approximately 4.5 is obtained for M1-transitions in this energy range. The binding energies for atomic electrons in the K, L and M shells in elements No and Lr are tabulated in table 1.1.

Table 1.1 Binding energies [keV] of atomic electrons in No and Lr.

Element	K	L_1	L_2	L_3	M_1	M_2	M_3	M_4	M_5
No	149.2	29.2	28.3	21.9	7.7	7.2	5.7	5.0	4.7
Lr	153.0	30.1	29.1	22.4	7.9	7.5	5.9	5.2	4.9

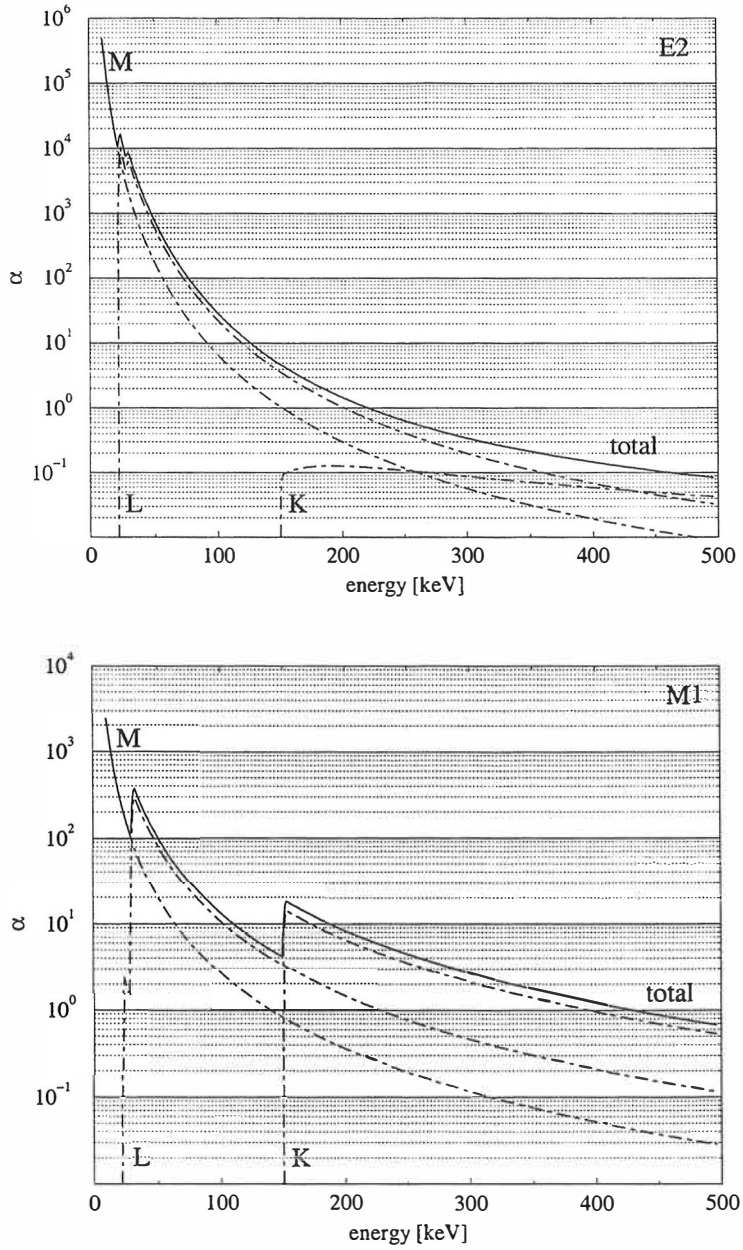

Figure 1.1 Total conversion coefficients and the contributions from K, L and M conversions for E2 and M1-transitions for nuclei with $Z = 102$.

The γ-ray transition probability strongly depends on the transition energy E_γ [MeV]. For an E2-transition it is

$$\lambda(E2) = 1.225 \cdot 10^9 E_\gamma^5 B(E2), \tag{1.11}$$

where $\lambda(E2)$ is given in s^{-1} and the reduced transition probability $B(E2)$ in e^2fm^4.

Transition probabilities calculated for pure single-particle transitions within the simple shell model are called Weisskopf estimates. For collective transitions, the reduced transition probabilities have been deduced by Bohr and Mottelson [Boh 75]. For E2-transitions it is

$$B(E2; I_i \longrightarrow I_f) = \frac{5}{16\pi} Q_0^2 |\langle I_i K_i 20 | I_f K_f \rangle|^2, \tag{1.12}$$

where Q_0 is the intrinsic electric quadrupole moment and K is the projection of the total angular momentum onto the symmetry axis. A simple expression for the intrinsic quadrupole moment is [Kra 88]

$$Q_0 = \frac{3}{\sqrt{5\pi}} R_{ave}^2 Z \beta_2 (1 + 0.16\beta_2), \tag{1.13}$$

where the deformation parameter β_2 is related to the eccentricity of the ellipse.

When inserting $R_{ave} = 1.20 \cdot A^{1/3}$ fm into equation (1.13) Q_0 can be approximated to

$$Q_0 \approx A^{2/3} \beta_2 Z. \tag{1.14}$$

When inserting this into equation (1.12), the transition probability (1.11) for the E2-transition becomes

$$\lambda(E2) \approx 1.225 \cdot 10^8 E_\gamma^5 A^{4/3} \beta_2^2 Z^2 |\langle I_i K_i 20 | I_f K_f \rangle|^2. \tag{1.15}$$

The Clebsch-Gordan coefficient for the transition from an initial state I to a final state $I-2$ is $\sqrt{\frac{1}{5}}$ in the case of $K=0$ and $I=2$. However, from an empirical fit to data [Gro 62, Ste 72], the following expression is obtained for the $2^+ \longrightarrow 0^+$ transition rates:

$$\lambda_\gamma(E2; 2 \longrightarrow 0) = (3 \pm 1) \cdot 10^{10} Z^2 E_\gamma^4 A^{-1}. \tag{1.16}$$

Equations 1.15 and 1.16 are used to extract an empirical formula for the quadrupole deformation parameter β_2:

$$\beta_2 \approx \left[\frac{1225}{A^{7/3} E(2^+)}\right]^{\frac{1}{2}}, \tag{1.17}$$

where the energy of the 2^+ state $E(2^+)$ is in MeV.

The excitation energy of approximately 40 keV was predicted [Mun 99] for the 2^+ state in ^{254}No resulting in a β_2 value of approximately 0.27. The E2-transition rate obtained by using equation (1.16) is approximately $3 \cdot 10^6$ s^{-1}. The total conversion coefficient for a 40 keV E2-transition in ^{254}No is approximately 2500, and therefore the total transition rate is on the order of 10^{10} s^{-1}. This leads to a half-life value on the order of 100 ps.

1.4 Production of the heavy elements

The only way to produce heavy elements is to use heavy-ion induced fusion-evaporation reactions. In these reactions, the projectile must penetrate the Coulomb barrier in order to fuse with the target nucleus. This barrier is a function of the charge and radius of the particles involved in the reaction. It can be expressed as

$$B_C = \frac{e^2}{4\pi\epsilon_0} \frac{Z_P Z_T}{R_P + R_T}, \tag{1.18}$$

where Z_P and Z_T are the proton numbers of the projectile and the target

nucleus with the charge-density radii R_P and R_T, respectively. By applying equation 1.1 for radii with the value of $r_0 = 1.45$ fm and by presenting the constant $e^2/4\pi\epsilon_0$ with its approximative value of 1.44 MeV·fm, B_C becomes

$$B_C = \frac{Z_P Z_T}{A_P^{1/3} + A_T^{1/3}} \text{MeV}. \tag{1.19}$$

A value of $B_C \approx 172$ MeV is obtained for the ^{48}Ca + ^{208}Pb system used to produce ^{254}No via the 2n fusion evaporation channel. In order to achieve fusion the projectile must overcome the fusion barrier. In the transuranium region the concept of "extra extra push" [Swi 82] requires a projectile energy several MeV higher than the Coulomb barrier itself. In general, a projectile energy of about 4.5 MeV/nucleon is needed.

After complete fusion the compound system has an excitation energy E^* which depends on the centre of mass energy E_{cm} of the colliding system and the Q-value of the reaction, where

$$E^* = E_{cm} + Q. \tag{1.20}$$

The compound system will rapidly "cool down" by evaporating neutrons and/or protons. The rest of the excitation energy is released in the de-excitations of the excited states of the final nucleus (e.g. rotation or vibration). In the present work the projectile and the target nuclei were selected in such a way that both Z and N are magic numbers or near magic numbers leading to relatively cold fusion reactions with low excitation energy. The Q-value in the reaction ^{48}Ca + ^{208}Pb $\longrightarrow$ ^{256}No* is approximately -155 MeV. Therefore, with a beam energy of 219 MeV the excitation energy of the ^{256}No compound nucleus is approximately 22.7 MeV. The neutron separation energy in ^{256}No is approximately 7.1 MeV resulting in an excitation energy of approximately 8.5 MeV in ^{254}No. Such a selection is important for the production of the heavy elements as their production cross-sections are low. Cold fusion gives the highest production cross-section and a clean reaction channel due to the fact that practically only one reaction channel is open.

Chapter 2

Spectroscopic methods

Due to the low production cross-sections of the heaviest elements ($Z > 100$), the main experimental information on their structure has been obtained in α-decay studies (e.g. [Müin 85] and [Heß 97]). In some cases β-decay and Coulomb-excitation studies are also possible [Sch 89]. In the present work heavy-ion induced fusion-evaporation reactions were used for in-beam studies of the ^{252,253,254}No and ^{255}Lr nuclei. In these types of reactions, fission dominates the total reaction cross-section leaving only a tiny portion ($\sim 10^{-6}$) to the fusion channels. Therefore special methods are needed to isolate transitions originating from the fusion products. A very selective way is to use recoil-gating and recoil-decay tagging (RDT) methods [Pau 95, Sim 86]. By employing these techniques it has been possible to perform in-beam γ-ray spectroscopic studies for nuclei with a production cross-section in fusion-evaporation reactions well below 1 μb [Jen 00].

2.1 Recoil Separators

A recoil separator is needed to collect and focus the nuclei of interest and to separate them from the primary heavy-ion beam and dominant fission products. Differences in the magnetic rigidities between these products allows in-flight separation by employing a magnetic dipole. In vacuum mode it is possible to reach high mass resolution but transmission of the system might be poor. Transmission suffers from the fact that the reaction products

have a wide range of charge states after passing through the target (Fig. 2.1). In order to collect the products with different charge states a large detector array would be needed. One of these vacuum-mode devices is the FMA (fragment mass analyzer) [Dav 89] located at the ATLAS accelerator at Argonne National Laboratory. It has been used succesfully in conjunction with the Gammasphere Ge-detector array in RDT measurements. The velocity filter SHIP [Mün 81] at GSI can select products within a certain velocity window. This allows the collection of reaction products with a wide range of charge states and therefore SHIP has a relatively high transmission. Both devices use combinations of electrostatic and magnetic fields.

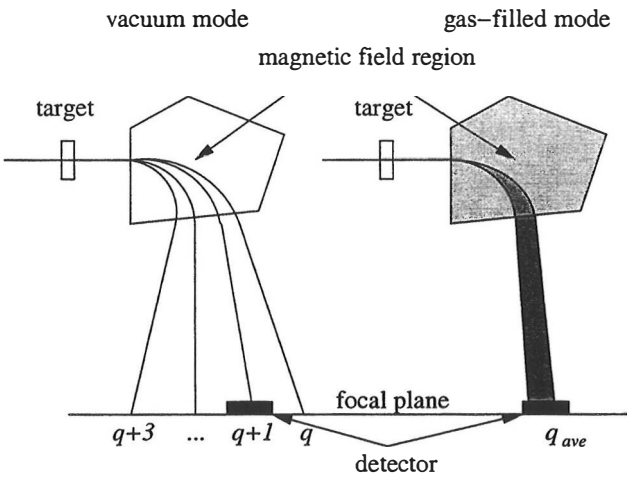

Figure 2.1 Schematic drawing showing the principal difference between vacuum mode and gas-filled mode of a recoil separator.

In gas-filled recoil separators the heavy ions penetrate a gas-filled region where they undergo atomic charge-changing collisions resulting in a mean charge state (Fig. 2.1). This allows the collection of different charge states while maintaining good beam suppression.

2.1.1 RITU gas-filled recoil separator

The RITU (Recoil Ion Transport Unit) [Lei 95] gas-filled recoil separator has three quadrupole magnets for focusing and one dipole magnet for separation. Its optical configuration is QDQQ (Fig. 2.2). Normally the volume from the target area to the RITU detector chamber at the focal plane is filled with dilute helium gas with a pressure of about 1 mbar. A regulated mass flow controller feeds helium gas into the target chamber, while pumping the separator vacuum chamber continuously. A thin foil (0.04 - 0.1 mg/cm^2) of carbon or nickel is used to separate the beam line and focal-plane detector from the gas-filled region.

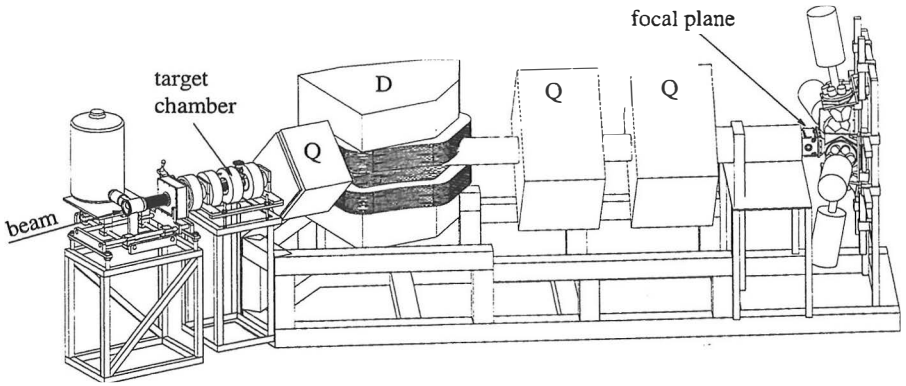

Figure 2.2 A schematic of the gas-filled recoil separator RITU. In this figure the target area is occupied by the SACRED electron spectrometer and the focal plane detector is surrounded by 4 Nordball Ge-detectors.

If the velocity v of the ion is in the range

$$1 < \frac{v}{v_0} < Z^{2/3},$$

where v_0 is the Bohr velocity ($2.19 \cdot 10^6$ m/s), the average charge state of the ion in the low-pressure gas is well defined:

$$q_{ave} \approx \frac{v}{v_0} Z^{1/3} \tag{2.1}$$

The magnetic rigidity of the ion in the gas-filled separator is then

$$B\rho = \frac{mv}{q} \approx \frac{mv}{q_{ave}} = \frac{mv_0}{Z^{1/3}} \approx 0.0227 \frac{A}{Z^{1/3}} \quad [\mathrm{Tm}], \tag{2.2}$$

which is only dependent on the mass number A and the proton number Z of the ion. Typical $B\rho$ resolution of the gas-filled recoil separator is $\frac{\Delta B\rho}{B\rho} = 10$ %. This does not allow the separation of the fusion products unambiguously, and therefore several different products are collected and focused to the focal plane detector. In this work, the velocities of No-recoils were approximately 2 % of the speed of light thus satisfying the required conditions.

Ions with magnetic rigidity up to 2.2 Tm can be separated by RITU [Enq 96]. The magnetic rigidity for the ^{254}No ions is about 1.2 Tm. Vertical and horizontal angular acceptances for RITU are ±80 mrad and ±30 mrad, respectively. The suppression factor for the full energy beam particles is on the order of 10^{12} - 10^{15}. The helium gas also works as an efficient cooler for the target allowing experiments with high-intensity beams. The mass resolution is poor but the transmission is very high depending on the symmetry of the reaction. Identification of a recoil is based on the study of its decay properties.

2.1.2 Decay spectroscopy

The transported fusion products are implanted into a position sensitive Si-strip detector at the focal plane of RITU (Fig. 2.3). The 300 μm thick 80 mm x 35 mm Si-strip detector is divided into 5 mm wide strips, each strip being position sensitive in the vertical direction. Typical vertical position resolution of the strip is 300 - 500 μm (FWHM) [Uus 96]. Normally the detector chamber vacuum is separated from the gas-filled volume of the separator so that the detector can be cooled to -20 °C to improve energy resolution. The typical implantation depth of a recoil is 2 - 5 μm depending on the recoil velocity and thus on the reaction symmetry. In the case of very asymmetric reactions the last foil separating the gas-filled volume and the detector chamber may need to be removed in order to get sufficient implantation depth. In this case it will not be possible to cool the detector. For a cooled detector,

typical energy resolution is about 30 keV for α-particles in the 8 MeV region.

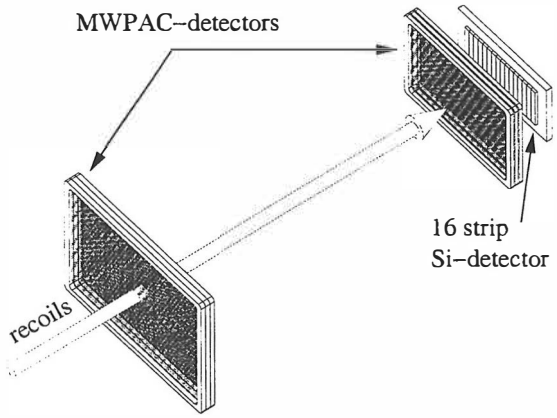

Figure 2.3 The focal-plane detector system at RITU is constructed from a 16 strip Si-detector and two multiwire proportional avalanche counter detectors (MWPAC).

The time of flight (TOF) (between the two MWPAC-detectors), energy and position of the recoil is recorded together with a time stamp of the recoil event. The TOF information can be used to clean the recoil spectra in order to reduce the amount of scattered beam and fission products. The implanted radioactive recoil may later decay via spontaneus fission, α, proton or β-decay or via other decay modes. The decay properties, e.g. α-decay energy together with position information and time stamp are also recorded. The observed decay events can be correlated with the recoils by looking backwards in time and requiring a recoil to occur at the same position as the decay. Identification of the recoil is then based on the known decay energy and half-life. The typical α-particle range in silicon ($E_\alpha \approx 8$ MeV) is approximately 50 μm which is much longer than the recoil implantation depth. As a result of this approximately 50 % of the decay events will escape from the detector. Therefore only part of the α-particle energy is observed and a wide "hump" of escaped α-events can be seen at the low energy region of the α-particle

spectra (Fig. 2.4).

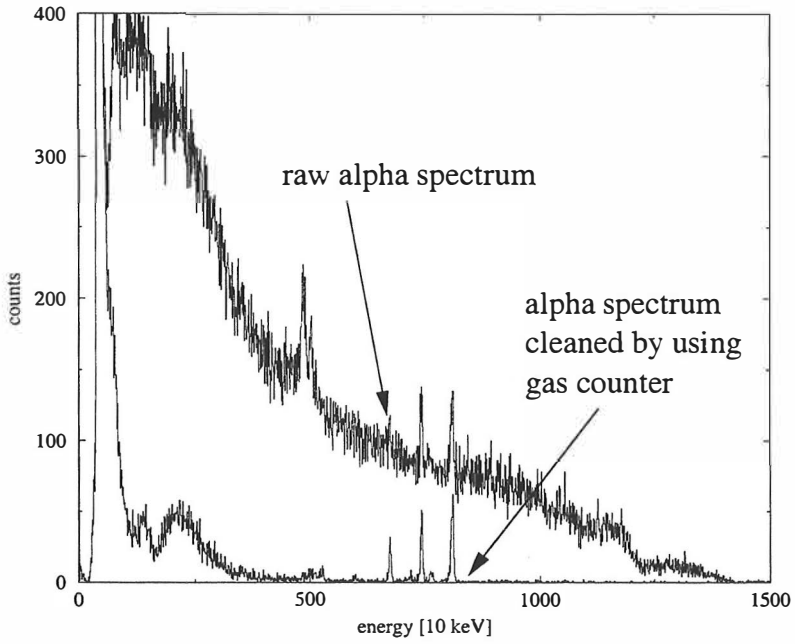

Figure 2.4 The raw α- particle spectrum can be cleaned by demanding that the gas counter (MWPAC-detector closest to the Si-detector) signal is not present. The spectrum is obtained at the RITU focal-plane detector from the $^{48}Ca + ^{208}Pb$ reaction.

In some cases scattered low-energy beam particles (overlapping with the α-decay energy range of interest) transported through the gas-filled separator may perturbate the α-particle spectrum. Furthermore, in many cases, the recoil energy may overlap with the α-decay energy range. A simple way to clean the α spectra is to use pulsed beam and record only those α-decay events which occur during the beam pause.

In order to avoid beam pulsing, a gas-filled multi wire proportional avalanche counter (MWPAC), was installed at the front of the strip detector [Ket 01]

(Fig. 2.3). The gas counter signal is used to veto events from the beam bursts resulting in a clean α-decay spectra (Fig. 2.4). Furthermore, low energy scattered beam often has a different energy loss in the gas counter than the recoils. This gives an additional condition for possible fusion product cleaning recoil spectra and reducing the number of accidental recoil-α correlations.

The MWPAC consists of three planes (cathode, anode and cathode, 110 mm $\times$ 64 mm) of thin ($\varnothing \approx 20$ μm) wires separated by 1 mm. The space between the cathodes is filled with 3 mbar of isobutane and 100 μg/cm^2 mylar foils are used to separate the different volumes. The distance between the cathodes is 8 mm. The anode voltage is typically +450 V and -50 V is supplied to both of the cathodes in order to shorten pulses. Short pulses are needed when running experiments at high counting rates. The time of flight (TOF) measurement system was later constructed from two MWPAC detectors (145 mm $\times$ 108 mm) separated by 300 mm (Fig. 2.3). Recoils and scattered beam can be separated due to the different flight time through the gas counters (Fig. 2.5).

2.2 In-beam gamma-ray spectroscopy

After formation of the compound system, the system is cooled down rapidly by particle evaporation and de-excitations in the final nuclei. These de-excitations mainly proceed via emission of γ-ray or conversion-electron cascades. Prompt γ-rays are emitted within one nano-second. To observe these prompt γ-rays the target area must be surrounded by γ-ray detectors. In the case of isomeric states, the nucleus may remain excited when passing through the recoil separator. The states populated in the decay of the isomer can be identified at the focal plane. In the present work, the flight time of the ^{254}No nuclei through RITU was approximately 1 μs. If the half-life of the isomeric state is of the order of 100 ns, the de-excitation of the states below the isomeric state may proceed inside RITU.

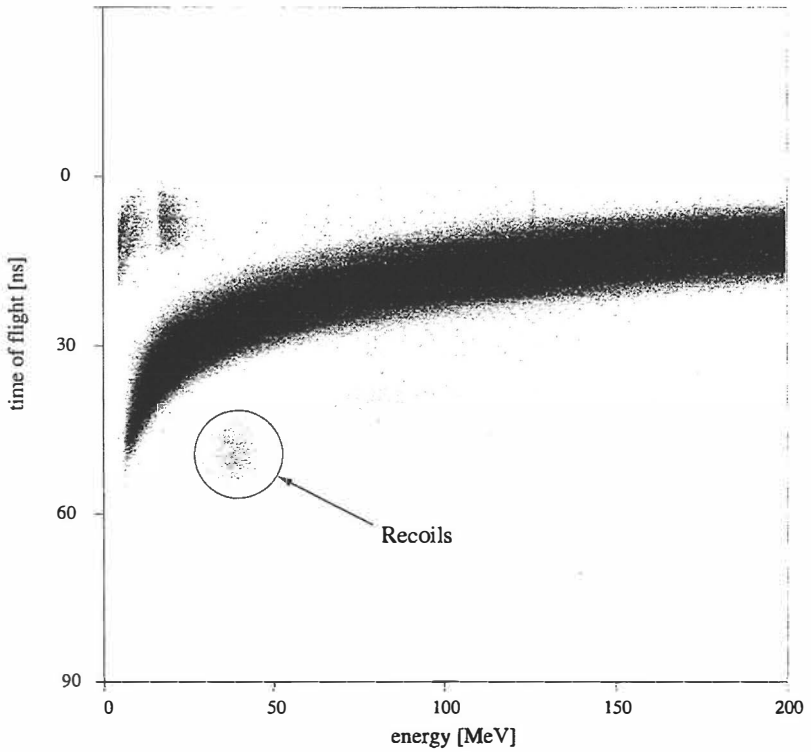

Figure 2.5 The time of flight system is able to separate the beam and the recoils. The banana-shaped structure corresponds to scattered beam particles. The ^{254}No recoils are seen below that structure due to the lower velocity. The time and energy calibrations are estimates based on calculated values for the recoils.

In this work different types of γ-ray detectors and detector arrays were used. High-purity Ge-semiconductor detectors were used to observe prompt γ-rays with high energy resolution, typically 2 - 3 keV for 1.33 MeV γ-rays. Compton scattering is the dominant type of interaction for 150 - 5000 keV γ-rays in the Ge-crystal. Most of the Compton-scattered γ-rays escape from the crystal. The resulting Compton background can be suppressed by surrounding the Ge-crystal with anti-Compton detectors. The peak-to-total ratio P/T for a typical Ge-detector with an anti-Compton shield used in this work was approximately 0.4 - 0.5 while without Compton suppression it was approxi-

mately 0.15.

The photopeak detection efficiency of a Ge-detector is normally given at E_γ = 1.33 MeV as a percentage of that for a 3 x 3 inch NaI(Tl) detector at a distance of 25 cm from a ^{60}Co source. The absolute photopeak efficiency of the 3 x 3 inch NaI(Tl) detector at that distance is 0.12 %. To calculate absolute efficiencies at other distances, it is often enough to take into account only the solid angle correction. It is possible to reach an absolute efficiency of a few % with a small number of Ge-detectors if a close geometry set up is used. The disadvantages of such a set up are Doppler broadening and coincidence summing which limit the use of the array to relatively low-multiplicity studies. The experiments presented in this work are relatively low-multiplicity studies with rather low recoil velocities, an ideal case for the use of compact Ge-detector arrays.

At present, the Euroball array is the most efficient Ge-detector array. It consists of different types of Compton-suppressed Ge-detectors: 30 Eurogam phase 1-type of detectors, 26 Ge-clover detectors (4 crystals) and 15 Ge-cluster detectors (7 crystals) at various target to detector distances. The absolute photopeak efficiency of this array at 1.33 MeV is $\approx$ 10 %. Gammasphere is an American array consisting of 110 Compton-suppressed large-volume Ge-detectors with Compton suppression. In order to increase granularity and decrease Doppler broadening, 70 of the Ge-crystals have been segmented electrically into 2 D-shaped halves. The total efficiency is close to that of Euroball. Gammasphere was combined with the FMA at Argonne during the period 1997 - 2000 and used in RDT measurements.

2.2.1 Jurosphere-array

The Jurosphere array used at the target area of RITU in the present work is a combination of 15 Compton suppressed Eurogam phase I detectors [Bea 92] ($\varepsilon \approx 75$ %) and 10 Nordball [Mos 89] ($\varepsilon \approx 40$ %) and TESSA [Nol 85] ($\varepsilon \approx 25$ %) detectors. The Jurosphere frame consists of two parts, a Eurogam frame

for the 15 Eurogam detectors at backward angles and a POLYTESSA frame for the 10 Nordball and TESSA detectors (Fig. 2.6). Ten of the Eurogam detectors are positioned at an angle of 157.6° and five at 133.6° with respect to the beam direction. The Nordball and TESSA detectors are positioned at 79° and 101°. The distance between the target and the detector crystals is approximately 205 mm resulting in an absolute total photopeak efficiency of approximately 2.5 %. However, the measured photopeak efficiency was approximately 1.7 % due to the use of collimators.

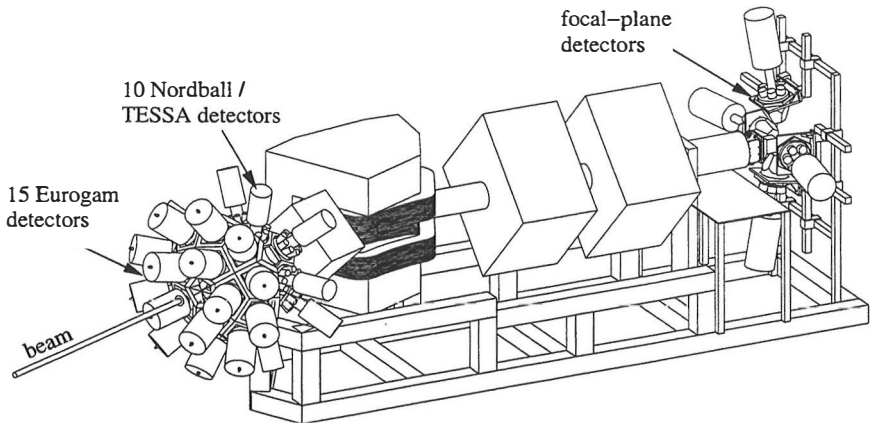

Figure 2.6 Schematic of the Jurosphere array combined with RITU.

A 40 μg/cm^2 carbon window separating the beam line vacuum and the gas-filled volume was positioned approximately 80 cm upstream from the target. A lead shield was used to reduce background radiation from the carbon window. The shield placed between the beam line and the 157.6° Eurogam detectors has a mass of about 50 kg (Fig. 2.7). The volumes separated by the fragile carbon window are pumped down carefully at a speed of about 1 mbar/s. In order to change targets the target chamber needs to be let up to air pressure. For this purpose the small valve downstream from the carbon window (Fig. 2.7) was closed and the volumes separated by the carbon window were kept under pumping during the process.

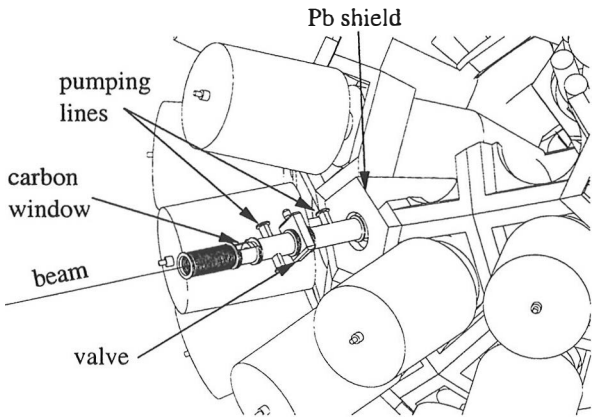

Figure 2.7 Lead shield used to protect the Ge-detectors against radiation produced at carbon window.

The universal Jurosphere target ladder allows the use of different types of target frames (Fig. 2.8). Typically two or three targets were mounted in the ladder with a viewer and an empty frame. The viewer was used to monitor the beam profile when focusing the beam. The empty frame and one empty position at the ladder were used to measure the possible background induced by the beam in the He-gas, the frame or the ladder. Counting rates were always checked with different combinations. In the heavy-element studies, the dominant background is normally due to the beam interacting with the He-gas.

2.2.2 SARI-array

After the first RDT campaign a SARI-array (Segmented Array at RITU) [Jon 99] replaced the Jurosphere array in the second campaign. This setup consisted of 4 segmented Ge-clover detectors [She 99], each mounted to the first quadrupole magnet of RITU at an angle of approximately $\theta = 50°$ with respect to the beam (Fig. 2.9). The crystal to target distance was 15 cm. The SARI-array was a compact array with detection efficiency similar to that of Jurosphere. However, the spectrum quality was poor due to the fact that the detectors had no Compton suppression shields.

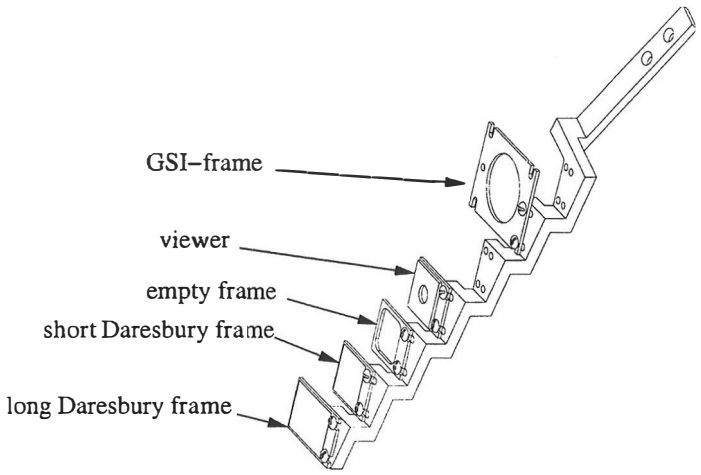

Figure 2.8 Universal Jurosphere target ladder.

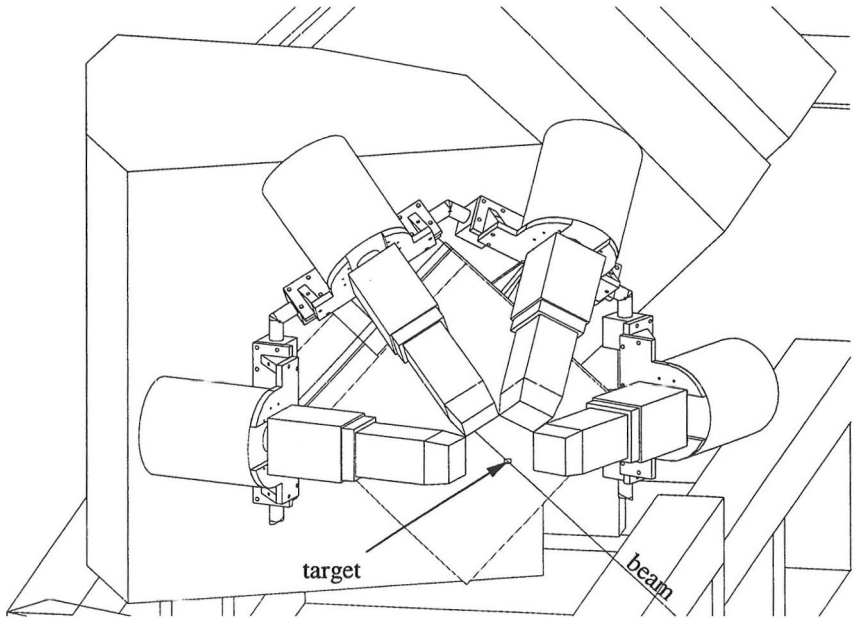

Figure 2.9 The SARI array was constructed from four segmented clover detectors mounted on the top of the first quadrupole magnet of RITU.

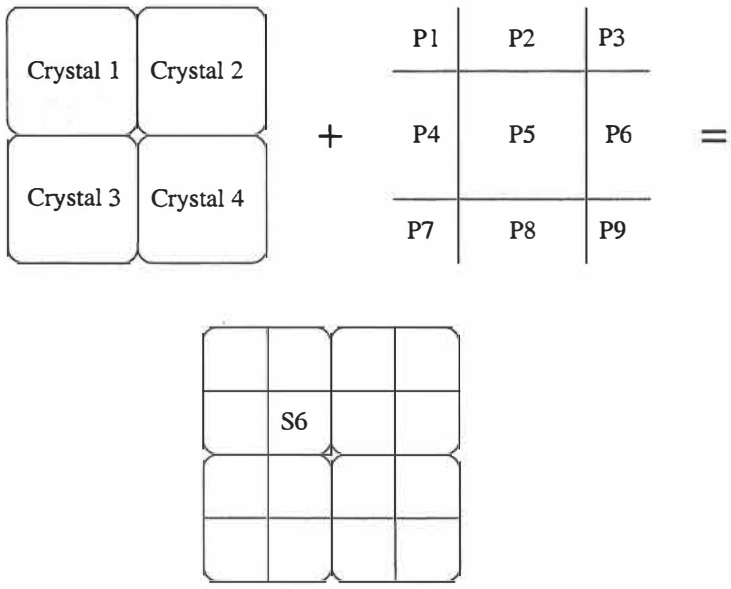

Figure 2.10 Segment recognition is based on the overlapping of 4 high energy crystal signals and 9 low resolution position signals. Due to the coupling of the position signals, only 68 out of 120 possible real two fold events look like a two fold event. The number of wrongly interpreted events grows dramatically for higher fold events – e.g. in reality there is only one event with all segments present but 1215 different combinations with real fold of 9 or higher leads to the same interpretation. The coupling limits the number of possible combinations to 1798 out of 65535 possibilities.

The segmented clover detectors were constructed from 4 individual Ge-crystals ($\varepsilon \approx 25$ %), each crystal electrically divided into 4 segments. The detector has 4 high resolution outputs, one from each crystals (Crystals 1 - 4 in figure 2.10) and 9 low resolution outputs from the segments coupled as shown in figure 2.10 (P 1 - 9). These two output-sets are used to recognise the segment that the γ-ray hit. Doppler corrections for the γ-ray energies in in-beam measurements are calculated with a θ-angle representing the centre of the recognised segment, and therefore Doppler broadening is reduced compared

to a non-segmented detector.

In the case of Compton scattering it is possible that the signal is registered in two or more segments. In that case the Doppler correction is calculated with an average θ-angle of the segments present. If a γ-ray scatters to a neighbouring crystal, the high resolution outputs from both crystals must be summed together (add-back mode). However, it is not possible to distinguish between the cases of two γ-rays hitting different segments and the scattering of a single γ-ray between these segments. In order to solve these kind of problems, more sophisticated methods are needed. Due to this reason only a simple add-back scheme was used in this work; only those events where two adjacent segments were present were accepted. These events were interpreted as a single γ-ray scattering from one segment to another. If two nonadjacent segments are present (e.g. opposite corner segments), the event is interpreted as a double γ-ray event. These condition requirements dramatically limit the total number of segment combinations. Most of the double γ-ray events (86 out of 120 combinations) are rejected or interpreted as a scattered single γ-ray event due to the coupling of the segments (Fig. 2.10). For this reason, the relatively close-geometry set-up of clover detectors used in the present studies is not suitable for cases of high γ-ray multiplicity. Part of the poor spectrum quality is due to the add-back mode, which was used to increase the efficiency of the array. The add-back factor was estimated to be approximately 1.3. The total absolute photopeak efficiency of the SARI-array at 1.33 MeV when using this add-back factor can be estimated to be

$$\varepsilon_{tot} = 4 \cdot \frac{4 \cdot 25\ \%}{100\ \%} \left(\frac{25\ \text{cm}}{15\ \text{cm}}\right)^2 \cdot 1.2 \cdot 10^{-3}\ \% \cdot 1.30 \approx 1.7\ \%.$$

2.3 Conversion electron spectroscopy

In the heavy nuclei studied in this work, the low-energy transitions mainly proceed via internal conversion. Therefore it is important to develop electron-spectroscopic methods for experimental studies of the structure of these nuclei.

Problems in conversion-electron spectroscopy arise from the fact that the detector and the source (or the target) must be placed in the same vacuum chamber. The electron detectors are sensitive to all kinds of radiation and therefore magnets are needed to transport conversion electrons further away from the source or target. More severe problems arise from the dominant delta-electron background in in-beam experiments. Electrons emitted in the decay of short living isomeric states ($\tau_{1/2} \approx 1$ ns) can be observed easily by using a recoil-shadow technique [Bac 78], but for detection of prompt conversion electrons with a broad range spectrometer, special methods are needed for suppression of the delta-electron flux.

Different types of magnetic spectrometers can be used to transport electrons from the source to the detector. A lens type of spectrometer can be constructed from solenoidal coils. In this spectrometer the field profile has typically two maxima, at the source and at the detector positions. Baffels in the low field region are used to suppress positrons and low-energy electrons. The momentum window of the lens type of device is selected by adjusting the current in the coils. A wide energy range is achieved by sweeping the current between two selected values. An orange type of spectrometer has a toroidal type of field and it can also be constructed from permanent magnets (mini-orange). Due to the limited momentum window, the lens spectrometers are not suitable for detection of electron-electron coincidences. For this reason they are normally operated with one single detector.

A solenoidal magnetic field is needed for broad-range detection of electrons. In the solenoid mode transmission of the spectrometer is only limited by the diameter of the bore of the solenoid and the field strength. It is possible to reach high detection efficiency of electrons up to ≈ 5 MeV in energy by using a superconducting solenoid magnet and a thick single Si(Li) or Ge-detector. In the broad-range mode coincidence measurements can be carried out by using segmented electron detectors. A picture of the SACRED (Solenoid and Array for ConveRsion Electron Detection) electron spectrometer designed

and constructed by P.A. Butler et al. [But 96a] is shown in figure 2.11. A 25 element 25 × 25 mm square matrix of PIN silicon detectors were used for coincidence measurements. Detection efficiency is limited at higher energies by the detector thickness. An electrostatic high voltage (HV) barrier is used to suppress the dominant low energy delta-electron background in prompt measurements. In this system, the solenoid axis is perpendicular to the beam axis.

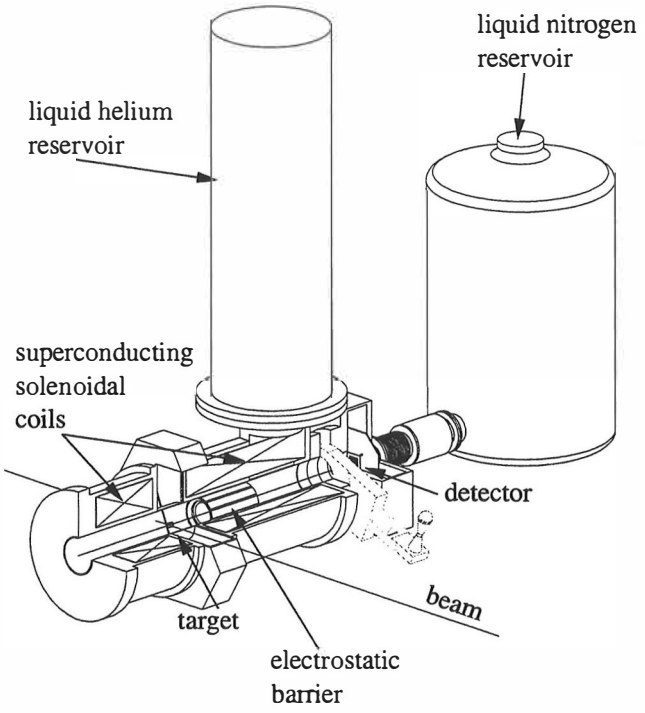

Figure 2.11 A schematic of the superconducting electron spectrometer SACRED.

To minimize Doppler broadening and the flux of disturbing delta-electrons induced by the beam in the target it is preferred to use collinear geometry, i.e. to align the solenoidal field with the beam and locate the detector near 180° with respect to the beam.

2.4 Collinear conversion electron spectrometer

In the present work the SACRED spectrometer was redesigned for use in collinear geometry in in-beam measurements at the RITU gas-filled recoil separator (Figs. 2.12 and 2.2). In a perfect collinear geometry the beam passes through the electron detector and therefore an annular detector with a hole at the centre is needed. This would require a hole size of approximately 10 mm in diameter when using cyclotron beams. According to the simulations described in [But 96a], this would significantly reduce the detection efficiency for low-energy electrons. For this reason, a tilted geometry was chosen where the solenoid axis is at an angle of 2.5° to the beam axis intersecting at the middle of the target.

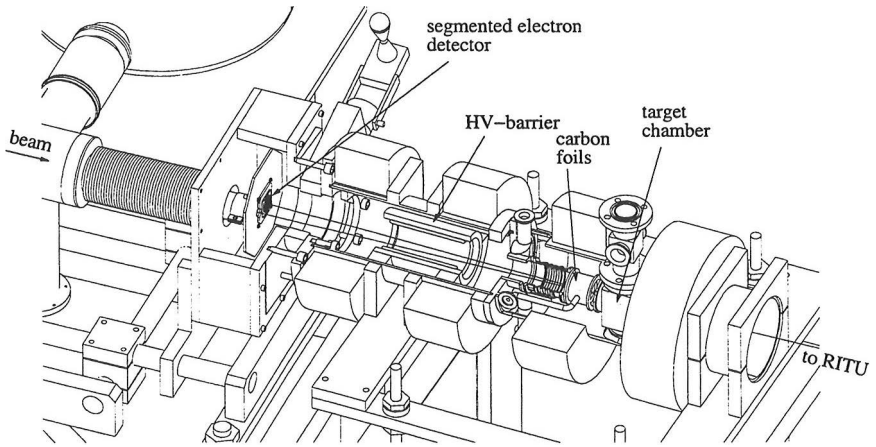

Figure 2.12 The SACRED electron spectrometer designed for the use in conjunction with the RITU gas-filled recoil separator.

In the newly configurated SACRED spectrometer a silicon PIN detector is

placed at a distance of 560 mm from the target. This circular detector with a diameter of 27.56 mm is segmented with 6 quadranted annuli surrounding the central element (Fig. 2.13). This provides 25 individual detector elements. The depletion depth of the detector is 500 μm at the operating bias voltage of 100 V. The detector as well as the first stage FET's for each element are mounted on a separate PCB. The bias voltage is applied via a 1 GΩ load resistance to the rear side of the detector which works as a common cathode. Each element has its own individual 761R preamplifier mounted externally to the vacuum box.

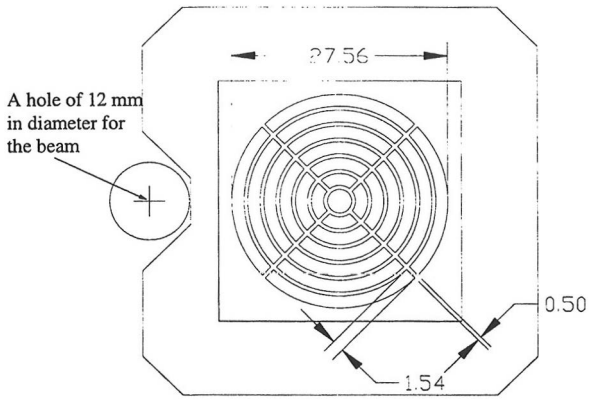

Figure 2.13 A layout of the segmented Si detector and the location of the 12 mm hole for the beam.

The detector is cooled to approximately -20°C in order to improve energy resolution. The cooling of the detector is achieved by thermal radiation from the rear side where a copper plate coated with a layer of carbon is placed in close vicinity (Fig. 2.14). The copper plate is cooled to approximately -150°C via a cold finger immersed in liquid nitrogen. This also acts as an efficient cold trap improving the vacuum conditions inside the detector chamber and in the HV-barrier volume. The current reading from an insulated copper collimator shown in figure 2.14 placed close to the detector was used to optimize the beam focus at that point.

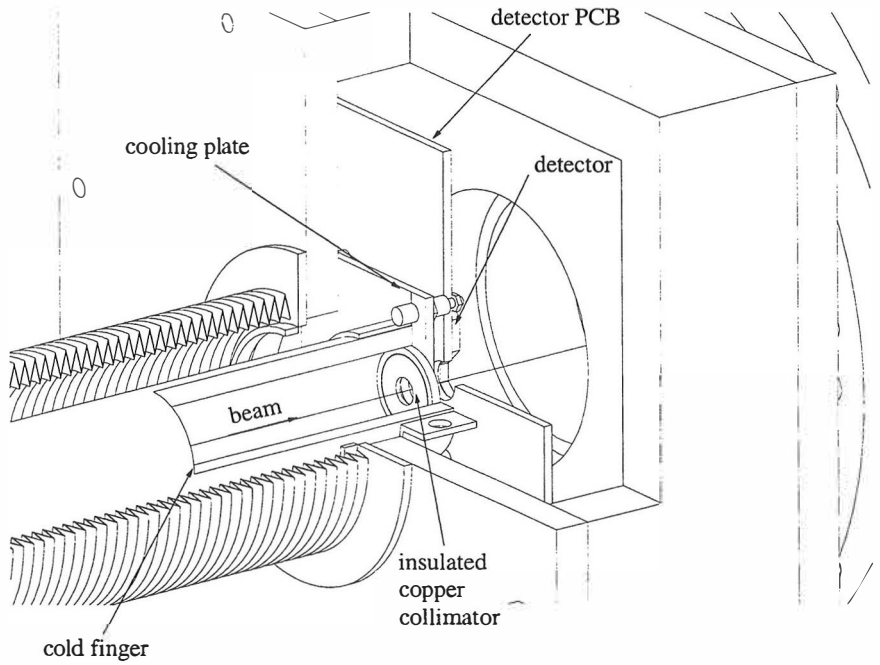

Figure 2.14 Cooling of the detector is achieved by thermal radiation from the rear of the detector. The cold finger is constructed from a hollow copper tube with an inner diameter of 29 mm. It is cooled by liquid nitrogen. The insulated copper collimator with a hole of 9 mm in diameter is used to optimize the beam focus at that point.

The HV-barrier is placed between the target and the detector (Fig. 2.12). In collinear geometry the beam passes through the HV-barrier and therefore the ionisation of the residual gas molecules by the beam generates electrons which are then accelerated by the electric field. These electrons are transported to the detector and for this reason the vacuum inside the HV-barrier must be as good as possible.

The gas-filled recoil separator RITU operates at a He pressure of about 1 mbar which makes the design of this type of spectrometer particularly dif-

ficult. With one 40 $\mu g/cm^2$ carbon foil as a gas window, it is possible to reach vacuum conditions of approximately 10^{-5} mbar behind the carbon foil. This is not enough, as the test experiments clearly showed a strong electron background in the case of poor vacuum conditions (Fig. 2.15). By using two separate carbon-foils with pumping of the intermediate volume (Fig. 2.16) it is possible to reach a pressure on the order of 10^{-7} mbar in the region of the HV barrier. This was found to be good enough to reduce the electron background to an acceptable level. The HV-barrier is displaced from the solenoid axis by 10 mm in order to avoid the beam hitting the edge of the barrier.

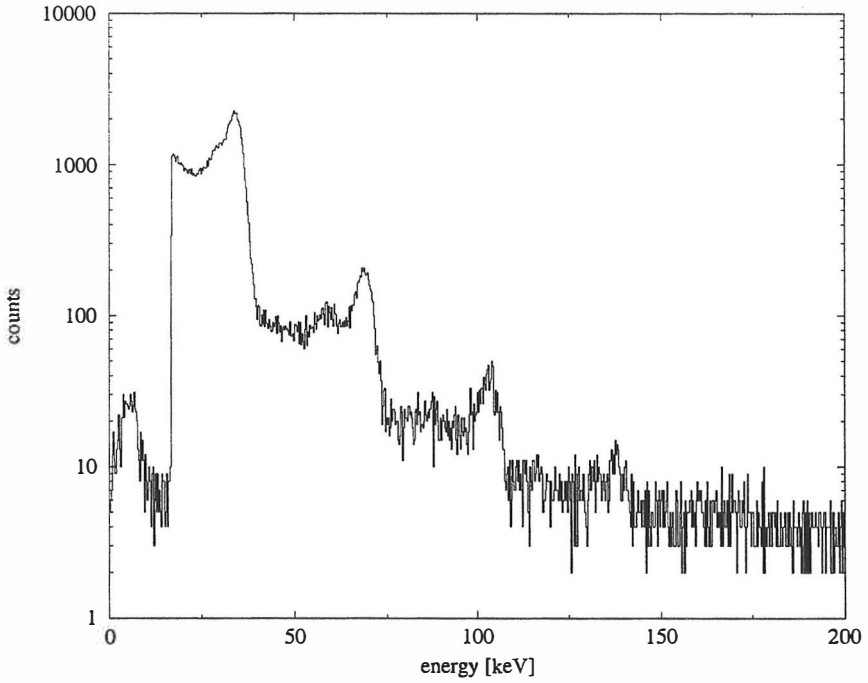

Figure 2.15 Background spectrum induced by the beam in the case of poor vacuum conditions inside the HV-barrier. The strong equally spaced structure corresponds to multiple hits of electrons with the energy of that of the HV-barrier voltage.

The three volumes separated by the carbon-foils must be pumped down si-

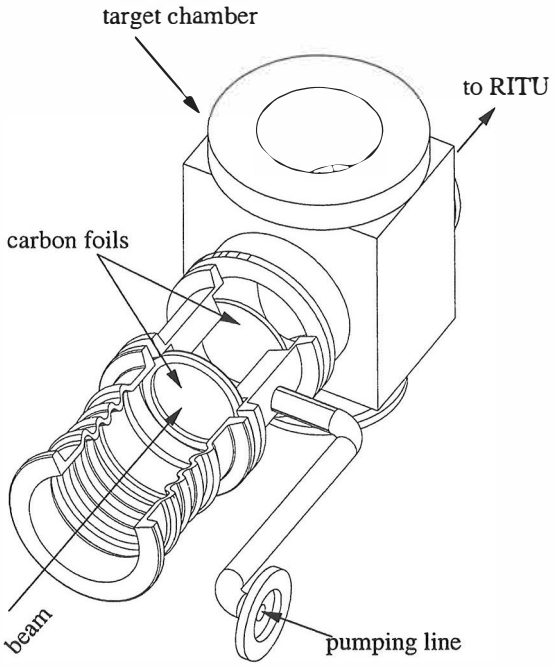

Figure 2.16 The recoil separator vacuum is separated from the electron-spectrometer by two 40 $\mu g/cm^2$ carbon foils placed upstream from the target chamber. The intermediate volume between the carbon windows is pumped by a separate pump.

multaneously. The pumping-down process is done through the volume on the detector side. The intermediate volume and the target chamber are connected to detector side volume (Fig. 2.17). A needle valve is used to maintain the pumping rate of 0.1 mbar/s. At the operational mode, the intermediate volume is pumped continuously by a separate pump. The vacuum inside the intermediate volume is approximately 10^{-4} mbar. The detector-side volume is pumped by a separate turbo-molecular pump to a pressure of approximately 10^{-6} mbar. Finally, cooling of the detector improves the detector-side vacuum to the required level. The second coil can be moved over the target position allowing easy replacement of the carbon foils.

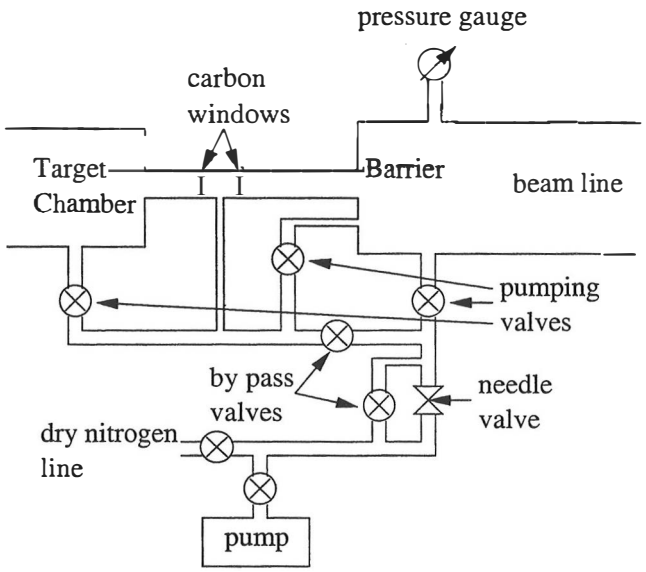

Figure 2.17 Scheme of the SACRED vacuum control system. Pumping speed is controlled by the needle valve and during the pumping down (letting up) processes all the pumping valves are open and the bypass valves closed. In the normal operational mode, all the pumping valves are closed and both of the bypass valves are open.

The solenoidal magnetic field is generated by four separate normal conducting solenoidal coils (Fig. 2.12). The coils with the inner diameter of 134 mm and the length of 87 mm are constructed from 10 × 8 loops made out of a 8.7 mm × 8.7 mm hollow copper tube, through which the cooling water passes. A safety interlock to switch off the power supply automatically in the case of cooling failure is constructed by monitoring the temperature sensors of the coils and the inlet water pressure. The coils are separated with spacings of 84 mm from each other. Each coil has the resistance of 20 mΩ and they are connected in series. The resulting magnetic flux density through the spectrometer is ≈ 0.3 T when the maximum current of 560 A is applied (Fig. 2.18). This is much lower than the maximum magnetic flux density of ≈ 2.0 T generated by the superconducting magnet of the earlier SACRED

spectrometer. This is still sufficient to transport electrons with energies <150 keV to the ø= 28 mm detector through the ø= 41 mm hole of the barrier without significant losses.

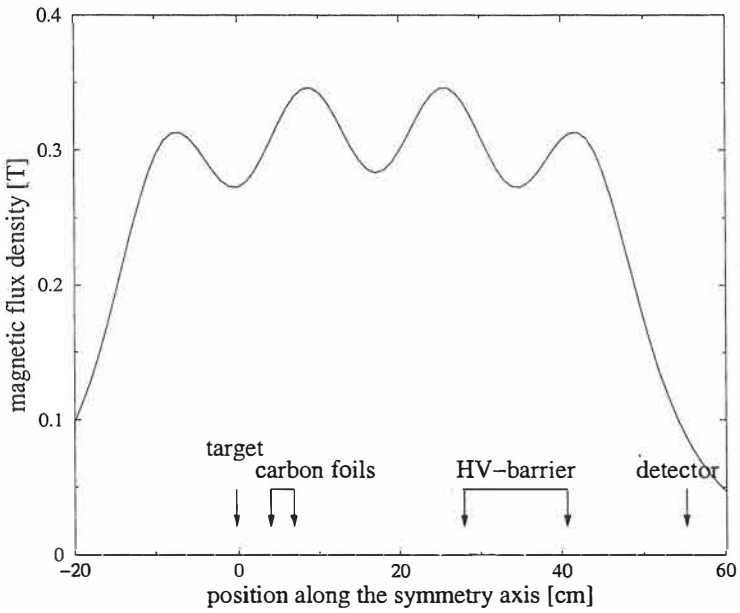

Figure 2.18 The calculated magnetic field profile at the centre of the solenoid axis and the relative positions of the target, the carbon-windows, the HV-barrier and the detector.

2.4.1 Performance

Resolution and detection efficiency measurements were carried out using an open 36 kBq ^{133}Ba source at the target position. Typical energy resolution (FWHM) for the 320 keV K-electron line of the 356 keV transition in ^{133}Cs was 3 - 4 keV. The total leakage current of the detector was 5 - 10 nA for the cooled detector. The two carbon foils separating the vacuum volumes had no visible effect on the energy resolution.

The absolute detection efficiency was determined for the strongest lines arising from transitions in ^{133}Cs (Fig. 2.19). The relative intensities of these transitions were taken from reference [Trz 90]. The drop in the efficiency curve at higher energies is due to the rather low magnetic flux density and the limited size of the detector. On the other hand, a higher magnetic flux density would focus low energy electrons towards the inner rings. This would lead to large differences in counting rates between the inner and outer elements. The detection efficiency is also reduced by the displaced HV-barrier and problems related to the precise alignment of the device. The counting rate distribution over the detector area for different electron energies is shown in figure 2.20. The right hand side of the detector is clearly shadowed by the HV-barrier, especially at higher energies.

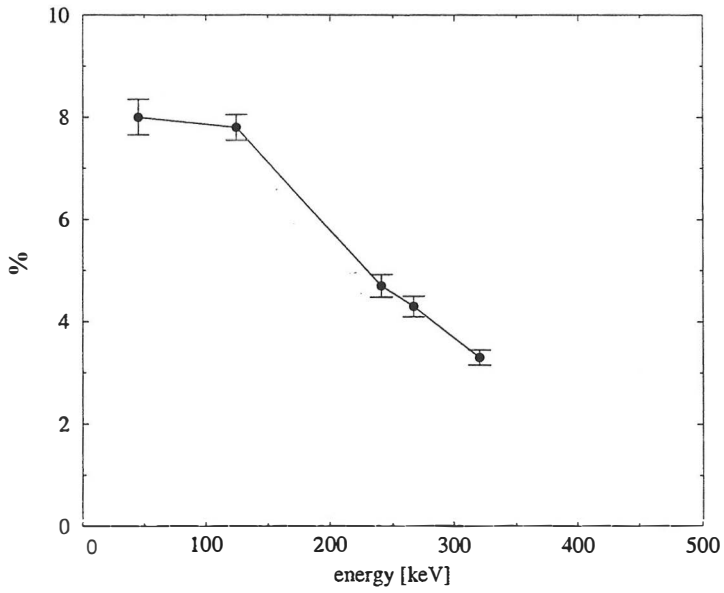

Figure 2.19 Absolute detection efficiency of the newly configurated SACRED spectrometer determined using a ^{133}Ba electron source.

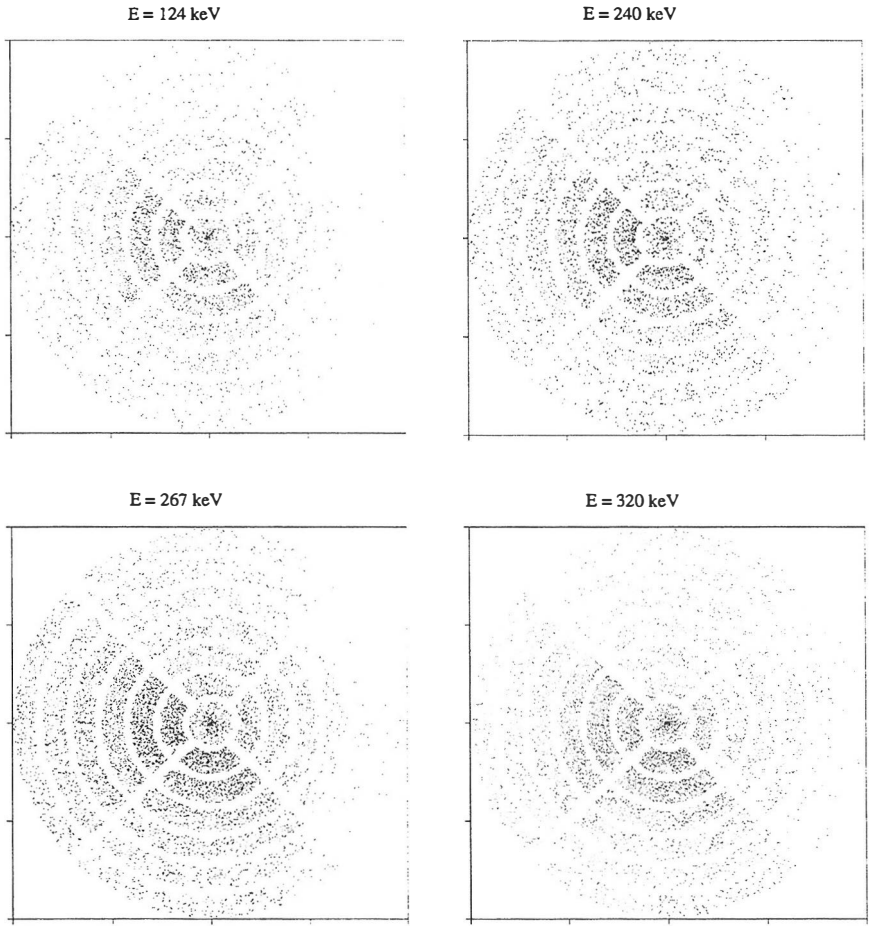

Figure 2.20 Counting rate distributions for the 124, 240, 267 and 320 keV electrons over the detector area. (See figure 2.13)

The in-beam test measurement was performed with a beam of 219 MeV ^{48}Ca on a 400 μg/cm^2 thick ^{124}Sn-target. The total irradiation time with a beam intensity of 0.4 pnA was 12 h. Total singles counting rates of the silicon array varied between 38 and 9 kHz with HV-barrier voltages from -20 kV to -35 kV, respectively. This is about 3 - 4 times less than that measured at the earlier SACRED setup with 0.5 pnA of 95 MeV ^{18}O beam

on a 250 μg/cm^2 thick ^{208}Pb target [But 96a]. This clearly shows that the delta-electron distribution is forward-peaking. Part of the background in the collinear geometry originates from the beam interacting with the residual gas inside the HV-barrier. This type of background was not present with the earlier SACRED setup.

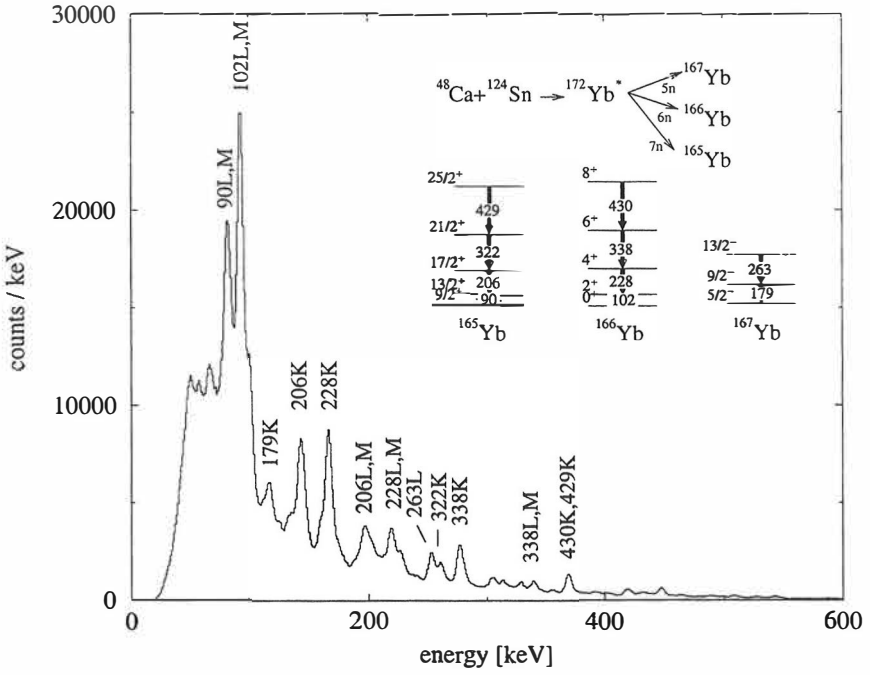

Figure 2.21 A recoil-gated singles electron spectrum from the ^{48}Ca + ^{124}Sn reactions. The K-conversion of the 263 keV transition in ^{167}Yb overlap with the L and M-conversions of the 206 keV transition in ^{165}Yb. The L-conversion of this transition is visible at the energy of about 253 keV partially overlapping with the K-conversion of the 322 keV transition in ^{165}Yb.

The yrast transitions in ^{165,166,167}Yb are clearly visible in the resulting recoil-gated electron spectrum shown in figure 2.21. A recoil-gated E_e - E_e matrix from this measurement is shown in figure 2.22. It clearly shows coincident

transitions in these nuclei. The diagonal lines are due to backscattered electrons which are reflected from the magnetic field back to another detector element. By gating on the K-line of the 430 keV $8^+ \longrightarrow 6^+$ transition in ^{166}Yb, the other transitions below this transition become visible (Fig. 2.23).

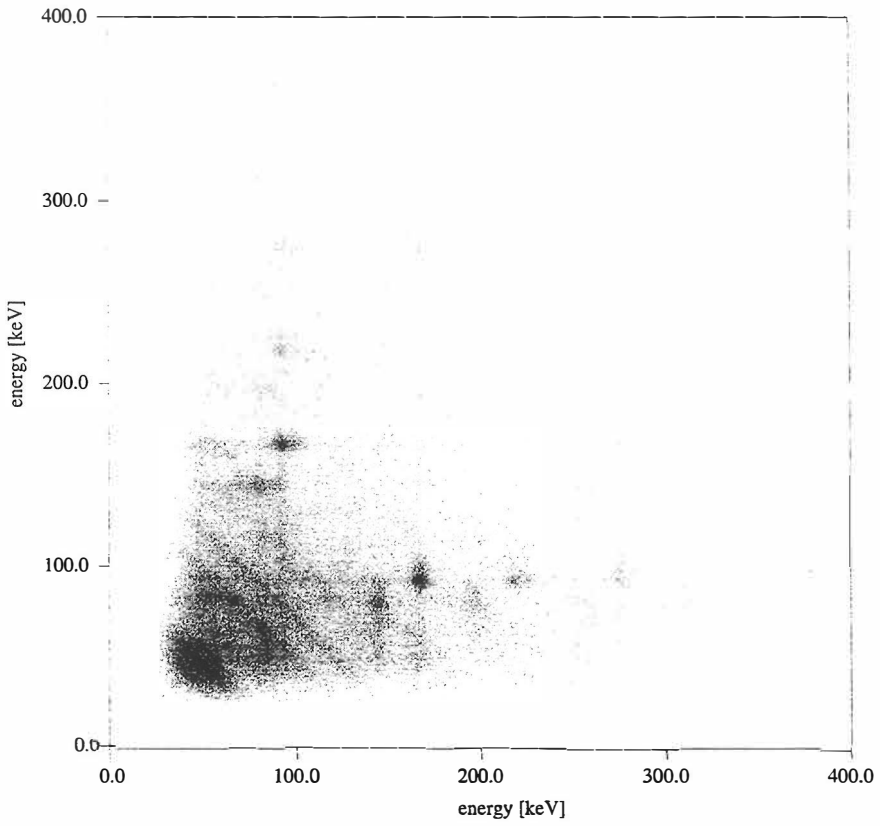

Figure 2.22 Recoil-gated E_e - E_e matrix showing the coincidences between the transitions in the ground state bands in ^{165,166}Yb nuclei.

In the collinear geometry the Doppler shift of the electrons emitted from a recoil must be taken into account carefully. Derivation of the equation for calculating unshifted electron energies from those measured for the peaks in the spectra is given in appendix A. Due to the poor timing properties

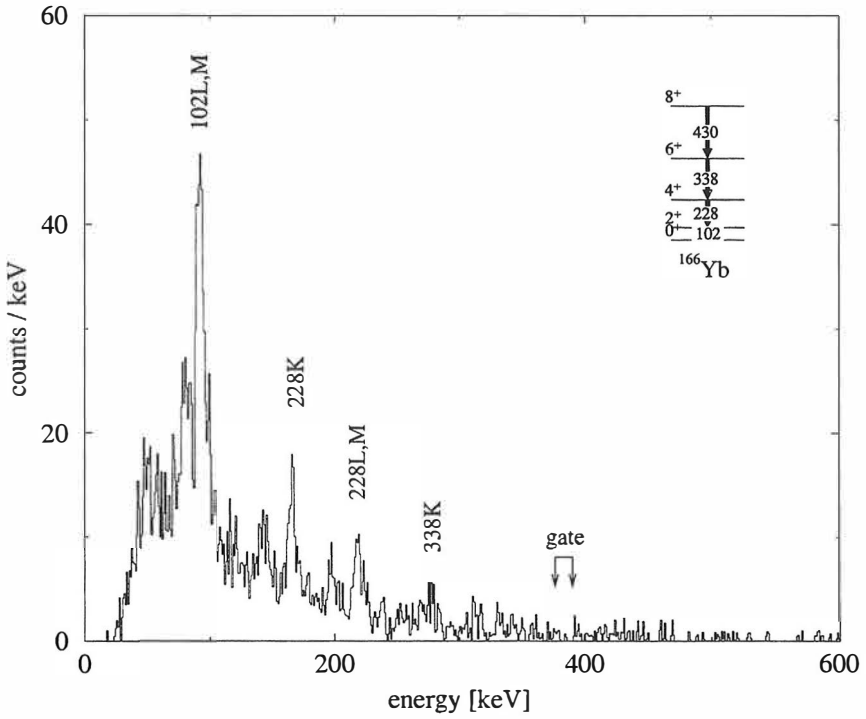

Figure 2.23 The yrast transitions in ^{166}Yb below the 430 keV $8^+ \longrightarrow 6^+$ transition. Some of the transitions in ^{165}Yb are still visible due to the 429 keV transition in this nucleus.

of the Si PIN detector, it is not possible to determine flight times of the electrons through the spectrometer, and consequently, not possible to distinguish between different emission angles θ' [But 96a]. For this reason only an average detection angle θ'_{ave} is used. In general, this is also energy dependent due to the backscattering probability and the geometrical limitations of the spectrometer. For the present SACRED spectrometer, the average detection angle is $\approx$ 150° - 160° for electron energies below 400 keV. By using the calculated value of $\beta \approx 0.027$c for the velocity of the Yb recoils, it is possible to define the average detection angle for electrons from ^{165,166,167}Yb using

$$\cos\theta'_{ave} = \frac{E' + m - (E+m)\sqrt{1-\beta^2}}{\beta\sqrt{E'^2 + 2mE'}}. \tag{2.3}$$

E and E' are the unshifted (known) and shifted electron energies, respectively. Average detection angles below 400 keV calculated from the most pronounced peaks in the spectrum of figure 2.21 are shown in figure 2.24. A straight line is fitted to the observed values. This line is used to define the Doppler correction angle for the observed electrons. The use of this method resulted in correct electron energies within 0.1 keV or less. A FWHM value of about 5.5 keV was measured for the 338 keV K-electron line from ^{166}Yb, indicating that the Doppler broadening is approximately 2 keV.

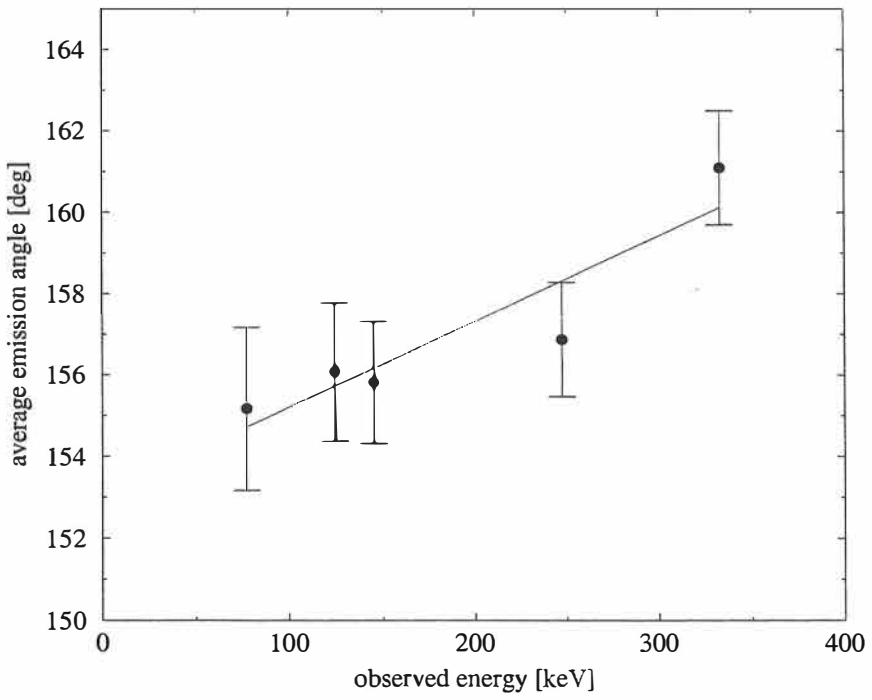

Figure 2.24 Average emission angle of the detected electrons for the identified peaks in Fig. 2.21. Doppler correction is calulated by using the (fitted) straight line.

Chapter 3

Electronics and data processing

The prompt events observed with the detector arrays at the target area are processed with standard NIM-based electronics. Separate electronics are used to record the recoil and decay events at the focal-plane of RITU. The correlation between recoil and decay events is based on the requirement that both of the events are observed at the same position in the position sensitive focal-plane Si-strip detector. The prompt events from the target-area detectors must be correlated with the recoil events at the focal-plane in order to utilise the recoil-gating as well as recoil-decay tagging techniques. The fusion products have approximately the same flight time through the recoil separator and therefore it is enough to add a constant delay to the prompt signals. This results in a prompt coincidence between signals from the target-area detectors and recoils.

3.1 Electronics for the arrays at the target area

The target-area detector arrays used in this work consist of several individual detectors which generate energy and timing signals (Fig. 3.1). The energy signal is formed in the linear amplifier (LA), which is digitized by the analogue to digital converter (ADC). A pile-up rejection logic is used to remove events where two signals occur in too short a time interval (for signal processing

needs). The first signal is rejected due to the distorted pulse shape of the piled-up signal, which delays the zero-cross-over point in the bibolar output of the LA. The second signal is rejected by the delayed busy signal of the first signal. The BGO anti-Compton shields used in the Jurosphere Ge-detector array provide a veto signal for Compton-scattered events.

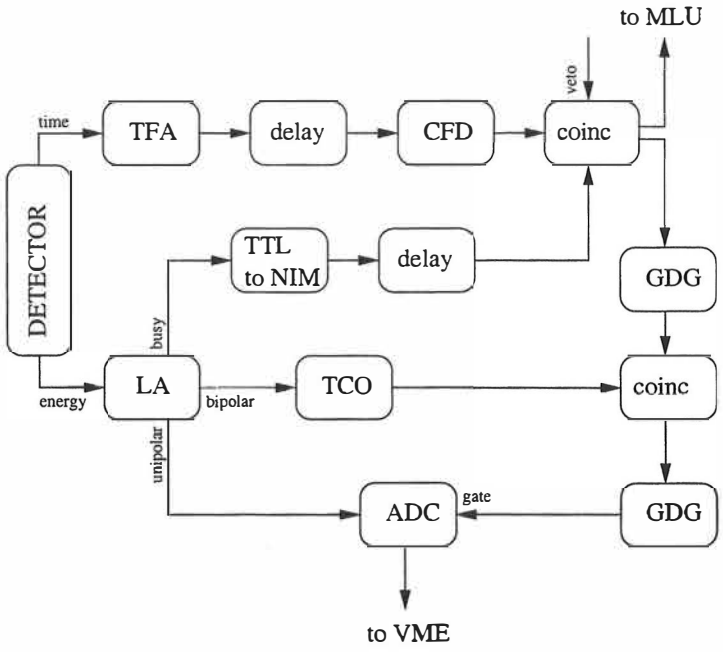

Figure 3.1 A block diagram of the target array detector logic.

The timing signals from the coincidence units are fed into a multiplicity logic unit (MLU) (Fig. 3.2). In this unit, a signal with an amplitude proportional to the number of overlapping timing signals is formed. The threshold of the MLU can be set for different coincidence folds depending on the experimental needs. It can then provide a common master-gate signal for the Event Manager which reads the ADC information only when this signal is present.

Furhermore, the MLU signal is used to form individual timing information

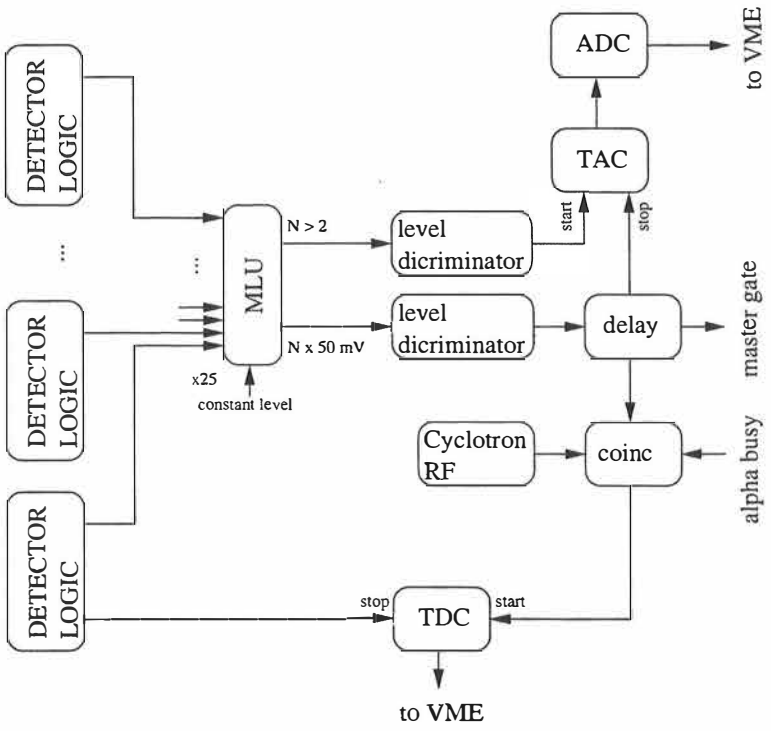

Figure 3.2 A block diagram of the TDC and TAC logic.

with respect to the cyclotron radio frequency signal (RF) i.e. against the beam pulse (Fig. 3.2). This time difference is digitized by a Time to Digital Converter (TDC). Several Time to Amplitude Converters (TAC) are used to record time differences between different events (e.g. prompt γ-ray against recoil event). The TAC logic corresponding to the time difference between two prompt γ-rays or electrons is shown in figure 3.2.

3.2 RITU electronics

The recoil and decay events are detected by the Si-strip detector at the focal plane of RITU. The signal strength at the end of the strip is dependent on the vertical position of the event, and therefore signals from both ends of

the strip are collected (top and bottom). The total energy (sum) is formed by summing the top and bottom signals. However, the sum energy signal is still slightly position dependent. The spectrum quality can be improved by calibrating the sum energy as a function of the position.

Due to the large energy difference between the recoil and decay events the signals are amplified with two different gain ranges. The high-gain amplifier is for the decay type of events and the low-gain amplifier is for the recoil type. A position calibration is needed to correlate the recoil events with the decay events. The delayed coincidence between the recoil event and the decay event is formed by requiring these events to occur in the same detector position within a certain time window (search time). This search time is typically set to approximately 4 half-lives of the nucleus of interest. For this reason, the average recoil implantation rate must be low enough in order to minimize the number of accidental correlations. Due to the position resolution of approximately 500 μm, the nominal number of detector elements is on the order of 1000. Taking into account the recoil distribution over the detector area, the effective number of detector elements is reduced to approximately 200. The recoil implantation rate is typically adjusted so that by taking this granularity, the average time difference for accidental recoil-decay correlations is on the order of 10 - 100 half-lives of the nucleus to be studied. A typical count rate of events classified as possible fusion products was approximately 0.36 Hz in the γ-ray experiment discussed in the section 4.1.1. This rate corresponds to an average time difference of approximately 10 half-lives of ^{254}No between implanted recoil events within the position window.

3.3 Data Acquisition

The data acquisition system is based on a set of VME crates. The read out controller reads out the ADC card information only when the master gate signal is present. An event builder collects data into a raw memory and when an event block is formed it is sent to a tape server. The acquisition

system is controlled by the MIDAS data acquisition control running on a SUN workstation.

The collected data were recorded on Exabyte tapes in Eurogam data format [Cre 91]. The recorded data are gathered into blocks (16384 bytes). Each of the blocks contains an identification header and an event block of variable length with several events. Each event block is terminated by the end block token which ensures that corrupted data do not infect the remaining blocks. The data are grouped so that all parameters related to a particular detector are kept together. The data parameter address is 14 bits long and it is divided into two parts, an 8 bit group number and a 6 bit item number. In standard Jurosphere experiments the group numbers 1 - 25 correspond to Ge- detector numbers 1 - 25, the first item being energy and the second item TDC. Each event has also a time stamp which is a 32 bit integer. With 1 μs time steps, an overflow of the clock occurs every $\approx$ 72 minutes.

3.4 RDT method

The prompt γ-ray or conversion electron events are delayed by the near constant flight time of the recoil through the gas-filled separator. This ensures that from the data acquisition point of view the recoil event and the prompt events are in coincidence. In general, only those prompt events that occur in coincidence with the recoil events are of interest and therefore a master-gate trigger is normally set to a recoil (or α-decay) event. Proper recoil-energy and flight-time conditions are used to gate prompt events. In this way only those events which originate from the nuclei of interest (fusion) are selected and the dominant background events (fission etc.) are suppressed. Prompt recoil gated events are dominated by the transitions from the nuclei of the strongest fusion evaporation channels.

In general, more than one fusion evaporation channel is open and therefore further selectivity is needed. Recoils can be properly identified on the basis

of their decay properties, e.g. α-decay energy and half-life. The known decay properties allow unambigious identification of the recoils. Prompt events that are in coincidence with correlated recoils originate from the nuclei selected by the decay requirements (RDT).

The analysis program allocates a space for a few thousand events. When there is an event which is a good candidate for a recoil (e.g. recoil energy and time of flight are correct) the event is stored in the stack which is automatically time ordered. When a decay event occurs the program starts to check the stack against the recoil and decay positions. When the position difference between the decay and the recoil event is within the selected window the recoil is correlated with the decay. Prompt events (γ-rays or conversion electrons) from the correlated recoil event are then taken to the RDT spectrum. The identified recoil event is removed from the stack in order to avoid multiple correlations to the same event.

Chapter 4

Experimental studies of No and Lr nuclei

As a result of fission, the cross-sections for producing heavy elements via fusion-evaporation reactions decrease rapidly when the proton number of the compound system increases. When doubly magic target and projectile nuclei are selected the excitation energy of the compound nucleus is relatively low and the fission probability is reduced. Due to this reason the ^{208}Pb(^{48}Ca,2n)^{254}No reaction has a large cross-section ($\sigma \approx 2$ μb) compared to any other reaction producing the ^{254}No nucleus. The neighbouring nuclei ^{252,253}No and ^{255}Lr can be produced using the ^{206,207}Pb and ^{209}Bi targets with cross-sections of a few hundred nb. A step of a few neutrons or protons further drops the reaction cross-sections by a factor of 10 - 100, well below the limit of any in-beam methods.

Techniques of recoil gating and recoil-decay tagging were utilised by employing the RITU gas-filled recoil separator. The Jurosphere and SARI arrays were used to perform in-beam γ-ray measurements for the ^{252,254}No and ^{255}Lr nuclei. In-beam electron spectroscopic experiments for ^{253,254}No were carried out using the collinear SACRED electron spectrometer.

4.1 Even-even No nuclei

The even-even ^{252,254}No nuclei are predicted to be deformed with a deformation parameter $\beta_2 \approx 0.25$ [Möl 95]. Therefore the lowest excited states of these nuclei are expected to be rotational, the 2^+ state lying about 40 keV above the ground state [Mun 99]. The de-excitation of such a low lying state should be highly converted with a conversion coefficient of approximately 1000. The expected γ-ray spectrum should consist of transitions with energies above $\approx$ 150 keV (transitions with total conversion below $\approx$ 10). As a sign of strong conversion of the low-energy transitions, strong No X-ray peaks should be seen. If the fission barrier is relatively low an instant cut-off of the rotational states should occur.

4.1.1 Gamma-ray and electron spectroscopic studies of ^{254}No

The first successful study of the excited states in ^{254}No was performed at the Argonne National Laboratory (ANL) in USA by employing the combination of Gammasphere and the FMA [Rei 99]. Transitions in the ground-state band were identified up to spin $I^\pi = 14^+$. Shortly after that a subsequent measurement at JYFL with the SARI-array (Fig. 2.9) was performed to confirm these results. The beam energy was chosen to be 219 MeV at the middle of a highly enriched (99 %) self-supporting 500 μg/cm^2 thick ^{208}Pb target enabling an extension of the ground-state band up to spin $I^\pi = 16^+$. This beam energy was approximately 4 MeV higher than that in the first ANL experiment. Another experiment at ANL was later performed with the same beam energy and transitions in the ground-state band were observed up to spin $I^\pi = 20^+$ [Rei 00].

In the JYFL experiment, two-weeks irradiation with a ^{48}Ca beam of 10 pnA yielded approximately 13500 α-decays of ^{254}No (Fig. 4.1). For ^{254}No, the decay modes are; α decay ((90 $\pm$ 4)%), electron capture ((10 $\pm$ 4)%) and spontaneous fission (0.25 %) [Rei 99, Tür 88]. Only one α peak with an energy

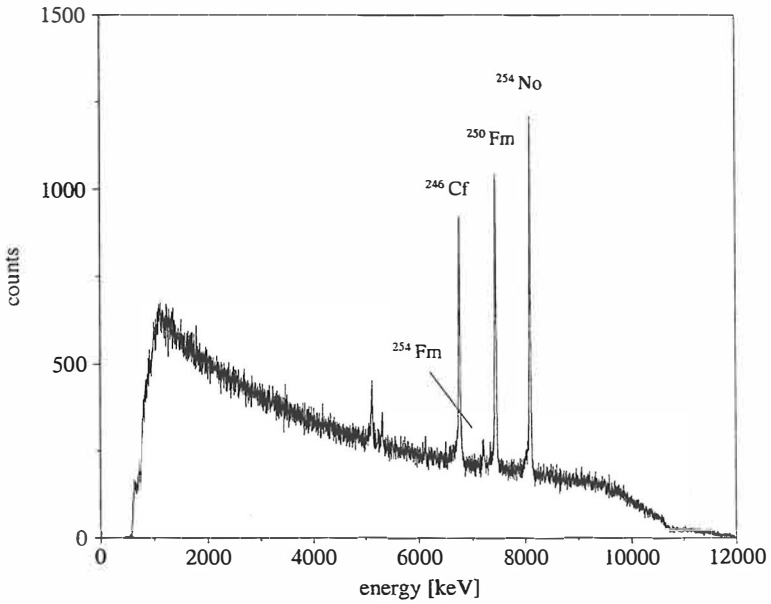

Figure 4.1 Total singles α-particle energy spectrum from the ^{48}Ca + ^{208}Pb reaction. The background is relatively high due to the fact that the gas-counter was not available in this experiment.

of 8093 keV is observed although approximately 15 - 20 % of the α decays of ^{254}No are expected to feed the first excited 2^+ level at approximately 45 keV in ^{250}Fm. However, the $2^+ \longrightarrow 0^+$ transition in ^{250}Fm is highly converted ($\alpha_{tot} \approx 1000$) and since the decaying nuclei are imbedded in the Si detector, the conversion electron energy adds to the α-particle energy forming a signal similar to that for a ground state to ground state α decay [Heß 89]. The three main α peaks in figure 4.1 belong to the α-decay chain of ^{254}No. The observed end-point of this α-decay chain is ^{242}Cm due to the relatively long half-life of approximately 163 days, thus far too long to be observed in the present experiment. The observed ^{254}Fm peak is due to the electron capture branch of ^{254}No. The α peaks around 5 MeV belong to long-living ^{208,210}Po isotopes produced in an earlier experiment.

Position information of the implanted recoil and α-particle events in the strip detector is deduced from the bottom to sum energy ratios. The two different amplification channels result in slightly different position information for the recoil and decay-event. Therefore each strip must be position-matched so that the same position information for the recoil and decay-events is obtained. After this procedure, a diagonal line between the recoil and decay-events is seen (Fig. 4.2). The width of the diagonal line corresponds to approximately 400 μm due to the finite position resolution of the detector and the α-particle range in the detector.

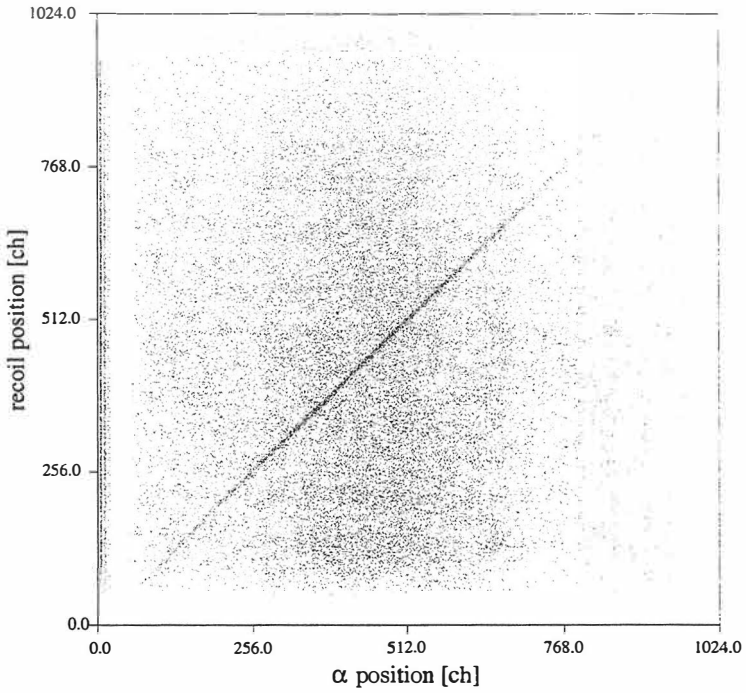

Figure 4.2 Position correlations between α-particles and possible fusion products implanted 0 - 150 seconds prior to the α-decay event. The diagonal line corresponds to the correct recoil α-particle correlation.

The time spectrum shown in figure 4.3 corresponds to the time-intervals

between the correlated recoils and α-decays which fall in the diagonal line in figure 4.2. The long-living component arises from random correlations, and the slope is determined by the total counting rate of the strip detector [Lei 81]. The short-living component corresponds to the real recoil-α-particle correlations with a half-life of 48 $\pm$ 3 s. The slight disagreement with the previously published value of 55 $\pm$ 5 s for ^{254}No is partly due to the time calibration used in [Ghi 67] which was based on the half-life of ^{214}Ra. It was later discovered that the Event Manager of the Data Acquisition system used in the present experiment holds the clock over the period it forms the event. For low data rates this should not have any influence on the half-life derived for ^{254}No.

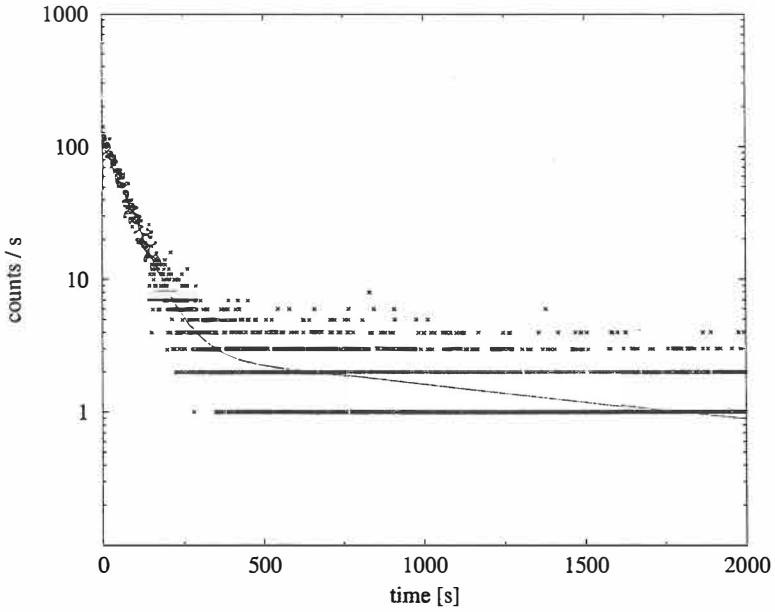

Figure 4.3 The distribution of ^{254}No recoil-α-particle time differences correlated at the same position in the Si-strip detector (diagonal line in figure 4.2).

The obtained recoil-gated and recoil-decay tagged prompt γ-ray spectra are shown in figure 4.4. In addition to No X-rays, six γ-ray peaks are observed

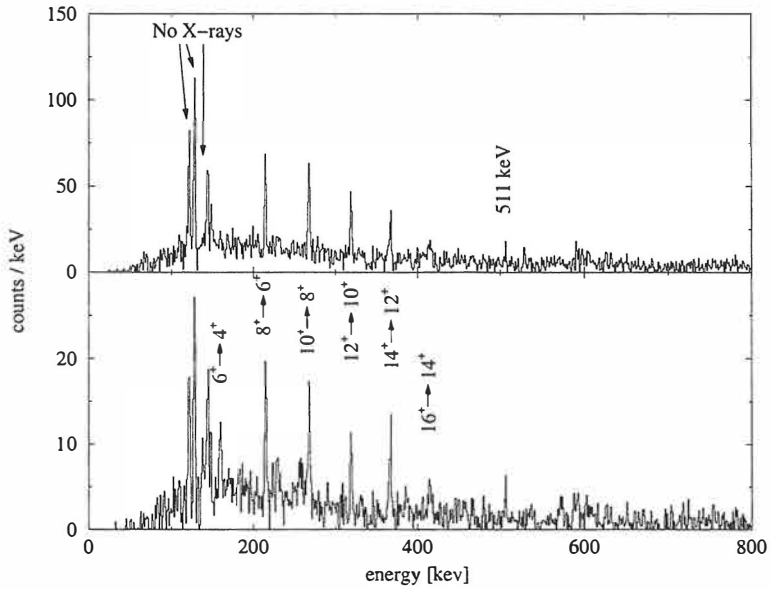

Figure 4.4 Recoil-gated (upper) and recoil-decay tagged (lower) spectra of prompt γ-rays from ^{254}No. The background is suppressed by using the background gate in the recoil-γ TAC. This reduces the intensity of the 159 keV $6^+ \longrightarrow 4^+$ transition due to a peak with similar energy in the subtracted background.

(Table 4.1). These peaks are assigned to an E2 cascade in the ground state rotational band of ^{254}No. The spins of the levels are assigned on the basis of the VMI method discussed in section 1.2 (Fig. 4.5). The Harris parameters with values of $\mathcal{J}_0 = 68.2\ \hbar^2/\text{MeV}$ and $\mathcal{J}_1 = 162.4\ \hbar^4/\text{MeV}^3$ were obtained from the fit in figure 4.5 representing a moment of inertia which increases slightly with the rotational frequency. The resulting level scheme for ^{254}No is shown in figure 4.6. The lowest two transitions were not observed in the γ-ray spectrum due to strong internal conversion. The transition energies (44.2 and 102.0 keV) of these transitions are extrapolated by using the fitted Harris parameters. By using the Harris parameters a value of 457 keV is deduced for the energy of the $18^+ \longrightarrow 16^+$ transition.

Table 4.1 The observed γ-ray transitions in ^{254}No and the level assignments. The intensities are normalised to 100 for the $6^+ \longrightarrow 4^+$ transition. The tabulated values for the conversion coefficients are used to extract $I_\gamma + I_e$.

E_γ [keV]	I_γ	$I_\gamma + I_e$	E_i	I_i [$\hbar$]	I_f [$\hbar$]
158.9(0.3)	20(6)	100(32)	305	6^+	4^+
214.1(0.3)	38(7)	84(16)	519	8^+	6^+
267.2(0.3)	47(8)	72(13)	786	10^+	8^+
318.2(0.3)	29(7)	38(9)	1104	12^+	10^+
366.5(0.3)	44(9)	53(11)	1471	14^+	12^+
414.0(1.0)	25(9)	29(10)	1885	16^+	14^+

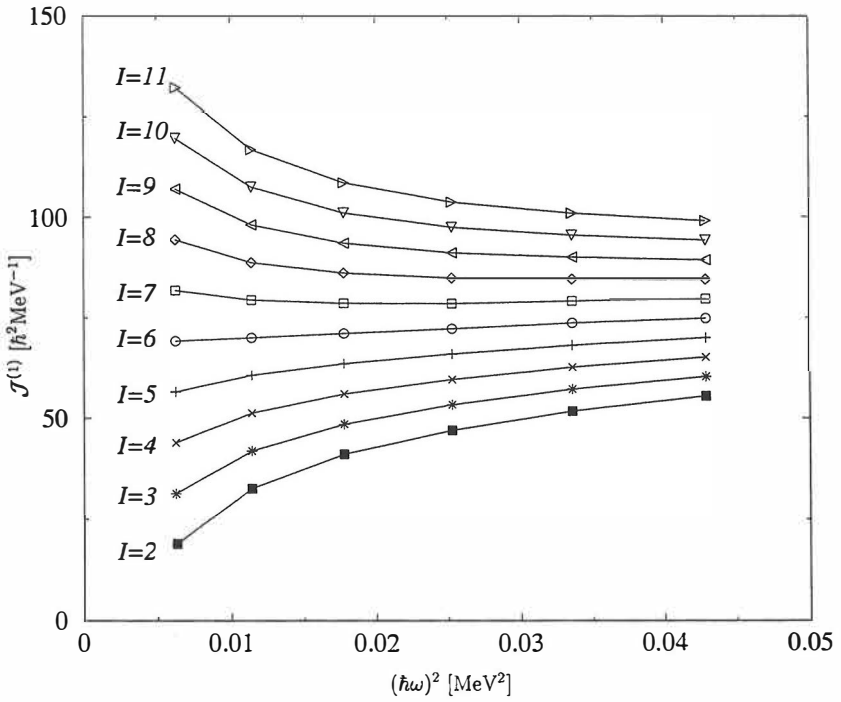

Figure 4.5 Plot of $\mathcal{J}^{(1)} = \hbar^2 \frac{2I-1}{E_\gamma}$ as a function of $(\hbar\omega)^2$ with different assumptions for spin values of the excited states in ^{254}No. The straight line ($I = 6$) corresponds to the correct assignment.

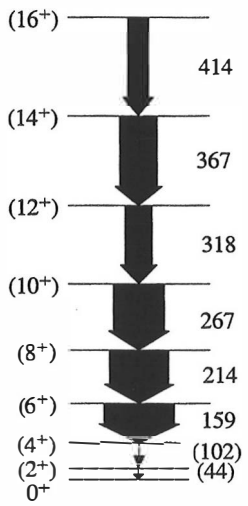

Figure 4.6 The proposed level scheme of the ground state band of ^{254}No. The line-widths correspond to the total transition intensity ($I_\gamma + I_e$ in table 4.1).

An attempt to observe low-lying states in ^{254}No was made by employing the collinear SACRED conversion electron spectrometer in conjunction with RITU (Fig. 2.2). The total counting rate of the electron detector was typically approximately 130 kHz with a ^{48}Ca beam of 3.5 pnA on a 430 μg/cm^2 thick ^{208}Pb target when a HV-barrier voltage of -40 kV was applied. The recoil-gated and recoil-decay tagged electron spectra shown in figure 4.7 were obtained in a 70 h experiment. Conversion-electron lines having energies of 74, 80, 96, 130, 138, 151, 186, 192 and 208 keV in the recoil-gated spectrum can be assigned to originate from L2, L3 and M (M2+M3) conversions of the $4^+ \longrightarrow 2^+$, $6^+ \longrightarrow 4^+$ and $8^+ \longrightarrow 6^+$ transitions in ^{254}No, respectively (Table 4.2). Observed relative intensities of these transitions are tabulated

in table 4.3. The L2/L3/M intensity ratios are close to those expected for E2-transitions in No (Table 4.2). The same peaks are also visible in the RDT spectrum (Fig. 4.7). Taking into account the total conversion coefficients for the $4^+ \longrightarrow 2^+$, $6^+ \longrightarrow 4^+$ and $8^+ \longrightarrow 6^+$ transitions in No, the relative total transition intensities derived from these spectra are 122, 100 and 65, respectively. These intensity values are comparable with those tabulated in table 4.1. This indicates that there is approximately 20 % side-feeding to the 4^+ state. Candidate peaks visible in both spectra with energies of 102, 108 and 133 keV cannot be associated with any of the transitions identified in the γ-ray study.

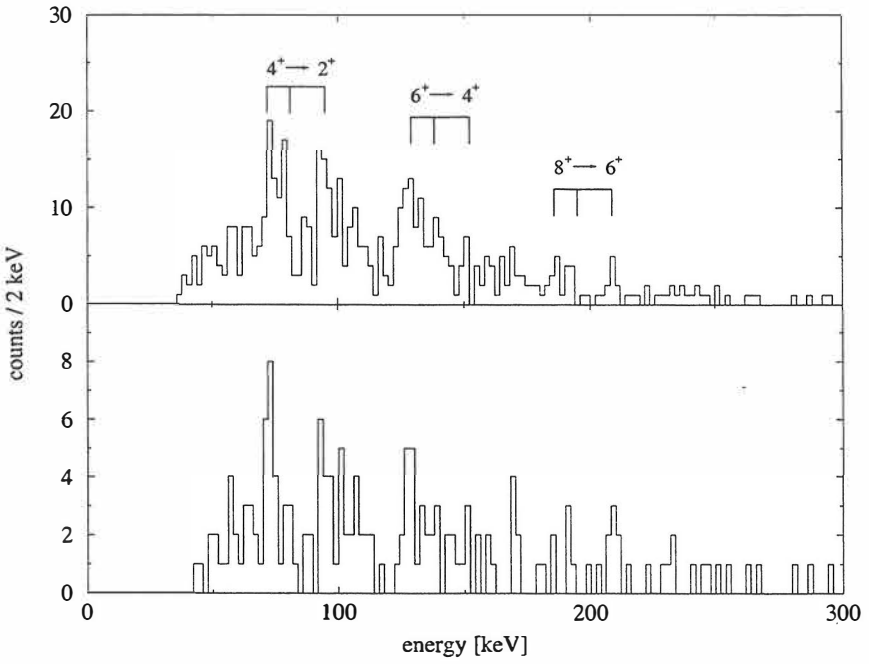

Figure 4.7 Recoil-gated (upper) and recoil-decay tagged (lower) electron spectra from ^{254}No obtained using the SACRED + RITU system. The marked lines correspond to L2, L3 and M conversions.

Table 4.2 Expected conversion-electron energies for low-lying transitions in ^{254}No ordered by conversion strength. Note that L2-conversion dominates for every transition. The K-conversion starts to compete with the L2-conversion above the transition energy of approximately 350 keV.

Transition $4^+ \longrightarrow 2^+$ $E_\gamma = 102.0$		Transition $6^+ \longrightarrow 4^+$ $E_\gamma = 158.9$	
E_e (shell)	α	E_e (shell)	α
73.7 (L2)	12.7	130.6 (L2)	1.81
80.1 (L3)	7.27	137.0 (L3)	0.83
94.8 (M2)	3.59	151.7 (M2)	0.51
96.3 (M3)	2.18	153.2 (M3)	0.25
100.1 (N2)	1.03	129.7 (L1)	0.19
Transition $8^+ \longrightarrow 6^+$ $E_\gamma = 214.1$		Transition $10^+ \longrightarrow 8^+$ $E_\gamma = 267.2$	
E_e (shell)	α	E_e (shell)	α
185.8 (L2)	0.51	238.9 (L2)	0.21
192.2 (L3)	0.20	118.0 (K)	0.10
206.9 (M2)	0.14	245.3 (L3)	0.07
64.9 (K)	0.12	260.0 (M2)	0.06
184.9 (L1)	0.08	238.0 (L1)	0.04

Table 4.3 Observed conversion-electron lines and their relative intensities normalised to 100 for L2-conversion of $6^+ \longrightarrow 4^+$ transition. The assignments are based on the information in Table 4.2.

E_e [keV]	I_e	line	I_i [$\hbar$]	I_f [$\hbar$]
74(2)	116(26)	102L2	4^+	2^+
80(2)	84(26)	102L3	4^+	2^+
96(3)	130(17)	102M	4^+	2^+
130(3)	100(21)	159L2	6^+	4^+
138(2)	55(20)	159L3	6^+	4^+
151(2)	31(10)	159M	6^+	4^+
186(2)	32(9)	214L2	8^+	6^+
192(2)	23(9)	214L3	8^+	6^+
208(2)	23(9)	214M	8^+	6^+

4.1.2 Gamma-rays from ^{252}No

An in-beam γ-ray study of excited states in ^{252}No was performed by employing the Jurosphere array in conjunction with RITU (Fig. 2.6). A highly enriched (> 99 %) 500 μg/cm^2 thick ^{206}Pb target was bombarded with a 20 pnA ^{48}Ca beam of 215.5 MeV at the middle of the target.

An irradiation time of approximately 10 days yielded $\approx$ 2800 α-particles from the decay of ^{252}No (Fig. 4.8). Other decay modes of ^{252}No are fission (20 %) and β^+-decay (23 %) [Ako 98] which were not detected. A cross-section value of about 300 nb was obtained by assuming a 25 % transmission for RITU. This cross-section value is in good agreement with the cross-section values determined in [Fle 76, Heß 85].

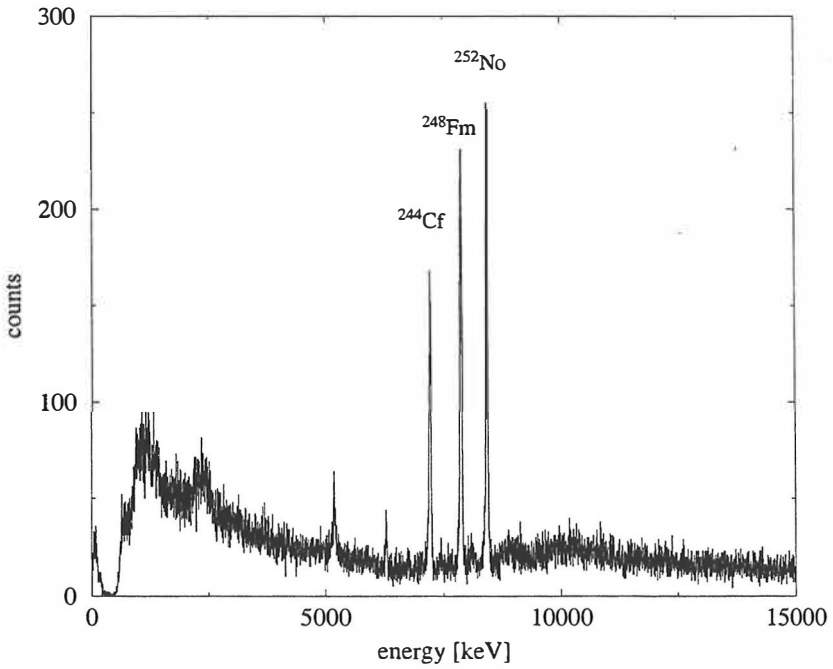

Figure 4.8 Total singles α-particle energy spectrum from the ^{48}Ca + ^{206}Pb reaction.

The ground state band in ^{252}No was identified up to spin $I^{\pi} = 16^{+}$ in the analysis similar to that in the study of ^{254}No. The recoil-gated and recoil-decay tagged γ-ray spectra are shown in figure 4.9. The six strongest peaks with energies of 166.9, 223.8, 277.2, 328.4, 375.5 and 416.7 keV were assigned to originate from an E2-cascade in ^{252}No (Table 4.4). Spin assignments based on the VMI fit discussed in section 1.2 resulted in the Harris parameters $\mathcal{J}_0$ = 64.2 $\hbar^2$/MeV and $\mathcal{J}_1$ = 227.6 $\hbar^4$/MeV^3. By extrapolating the Harris fit, energies of 46.4 and 107.4 keV were deduced for the $2^{+} \longrightarrow 0^{+}$ and $4^{+} \longrightarrow 2^{+}$ transitions, respectively.

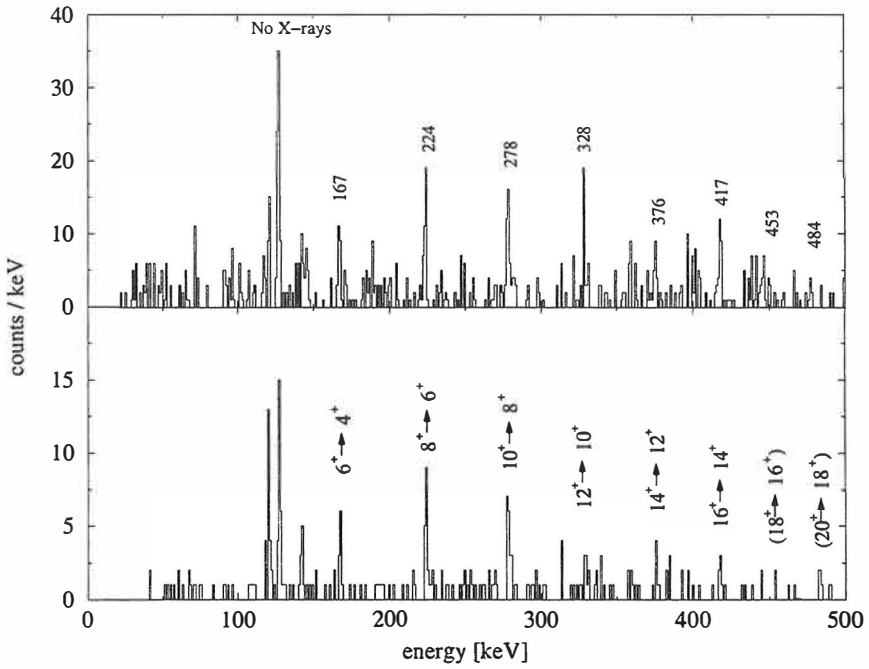

Figure 4.9 Recoil-gated (upper) and recoil-decay tagged (lower) spectra of prompt γ-rays from ^{252}No.

Suggestion for candidates for the $18^{+} \longrightarrow 16^{+}$ and $20^{+} \longrightarrow 18^{+}$ transitions

with energies of 453.2 and 483.7 keV were made on the basis of the recoil-decay tagged γ-ray spectrum. These transition energies are slightly lower than those extrapolated from the Harris fit, suggesting a small upbend in a plot of moment of inertia vs. transition energy. This observation supports the predicted neutron alignment effects in ^{252}No which should appear at the transition energy of approximately 440 keV [Lei 99]. The proposed level scheme for ^{252}No is shown in figure 4.10.

Table 4.4 Observed γ-ray transitions in ^{252}No and their level assignments. The intensities are normalised to 100 for the $6^+ \longrightarrow 4^+$ transition. The tabulated values for the conversion coefficients are used to extract $I_\gamma + I_e$.

E_γ [keV]	I_γ	$I_\gamma + I_e$	E_i	I_i [$\hbar$]	I_f [$\hbar$]
166.9(0.3)	23(7)	100(32)	321	6^+	4^+
223.8(0.2)	38(9)	77(18)	545	8^+	6^+
277.2(0.2)	62(11)	91(16)	822	10^+	8^+
328.4(0.3)	27(9)	34(11)	1150	12^+	10^+
375.7(0.4)	17(7)	20(8)	1526	14^+	12^+
416.7(0.4)	20(8)	23(9)	1943	16^+	14^+
(453.2(0.7))	8(6)	9(7)	2396	18^+	16^+
(483.7(0.7))	7(5)	8(6)	2879	20^+	18^+

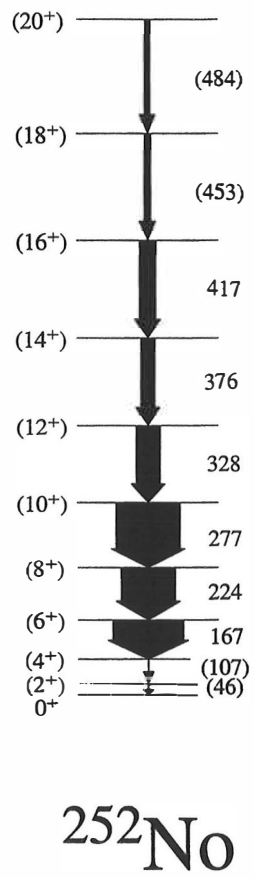

Figure 4.10 Proposed level scheme of ^{252}No.

4.2 Odd-A ^{253}No and ^{255}Lr nuclei

One goal in the study of heavy elements is to determine the ordering and excitation energies of the single-particle states near to the Fermi surface. The studies of even-even nuclei do not provide this information, and therefore identification of excited states in odd-mass nuclei is important. For ^{253}No and ^{255}Lr there are several possible configurations which could form the ground state. The expected γ-ray spectrum of yrast transitions from these nuclei can consist of E1, E2 and M1-transitions depending on the level ordering and their relative energies. If the configuration is such that the excited states de-excite mainly via M1-transitions (e.g. two closely spaced signature-partner bands) the de-excitations proceed mostly via internal conversion resulting in weak lines in the γ-ray spectrum (except strong X-rays).

4.2.1 Gamma-rays from ^{255}Lr

Recent calculations by S. Ćwiok [Ćwi 00] predict a $[514]\frac{7}{2}^-$ configuration for the ground state of ^{255}Lr. The next single-particle states are predicted to be $[624]\frac{9}{2}^+$ and $[530]\frac{1}{2}^-$ at excitation energies of approximately 68 and 135 keV, respectively. For the band above the $[514]\frac{7}{2}^-$ state, the de-excitations will proceed dominantly via a cascade of E2-transitions if ^{255}Lr is assumed to have a moment of inertia and deformation similar to ^{254}No. For the $[530]\frac{1}{2}^-$ configuration the coupling would probably lead to two almost degenerate signature-partner bands resulting in strong competition between M1 and E2-transitions. Similar competition between M1 and E2-transitions is predicted for the $[624]\frac{9}{2}^+$ configuration.

The Jurosphere experiment with a 10 pnA ^{48}Ca beam irradiating a 510 μg/cm^2 thick ^{209}Bi target over a period of approximately 10 days was performed. The bombarding energy of 221 MeV was used. The resulting α-particle spectrum is shown in figure 4.11. In total, approximately 2200 correlated recoil-α-particle pairs were observed.

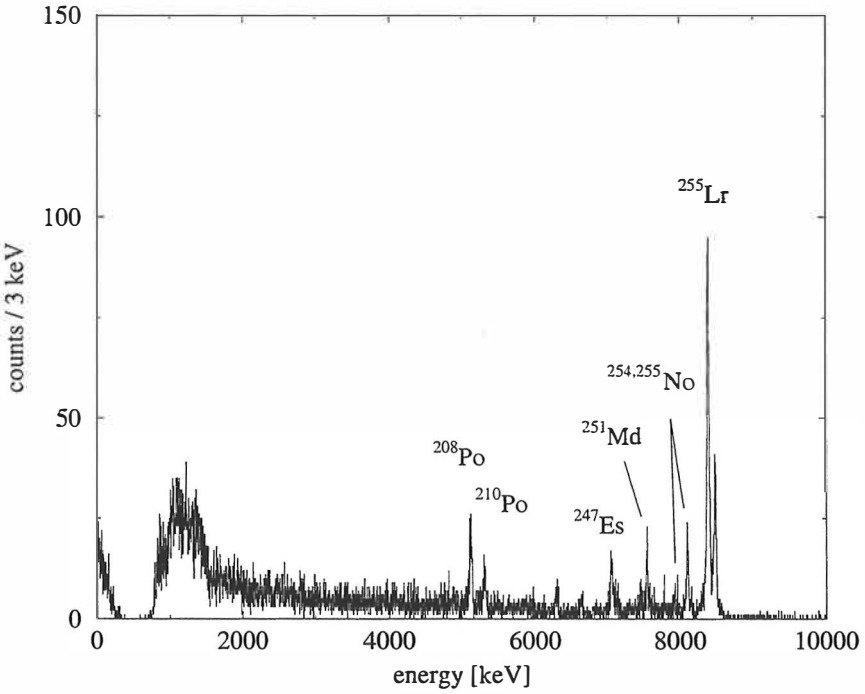

Figure 4.11 Total singles α-particle energy spectrum from the ^{48}Ca + ^{209}Bi reaction.

In the resulting recoil-gated γ-ray spectrum shown in figure 4.12, only Lr X-rays and one clear γ-ray peak at the energy of 247 keV is visible. This transition is still visible in the recoil-decay tagged γ-ray spectrum (Fig. 4.12). Based on this spectum, suggestions can be made for transitions with energies of 224 and 264 keV which are weakly visible in the recoil-gated spectrum. The number of γ-ray events compared to the intense Lr X-rays in the spectrum indicates that the yrast transitions in ^{255}Lr are of a highly converted M1-type. This suggests that the ground state configuration is unlikely to be $[514]\frac{7}{2}^-$. The total number of events in the recoil-gated γ-ray spectrum is low compared to the number of recoil-α-particle pairs which may be due to an isomer in ^{255}Lr.

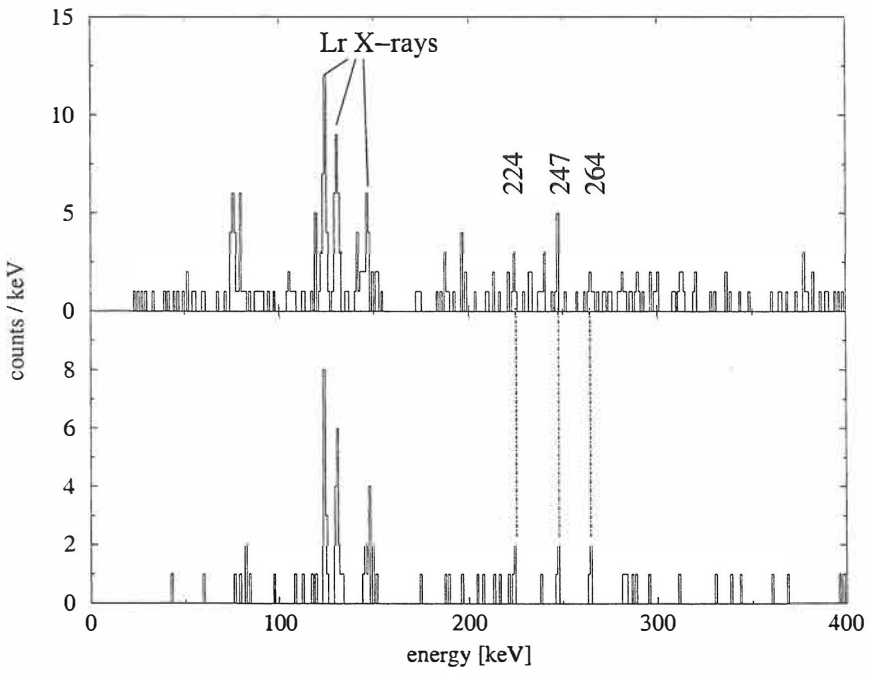

Figure 4.12 Recoil-gated (upper) and recoil-decay tagged (lower) spectra of prompt γ-rays from ^{255}Lr.

4.2.2 Electron spectroscopic studies of ^{253}No

According to cranked Wood-Saxon codes the ground state of ^{253}No should be based on the $[734]\frac{9}{2}^-$ configuration. The next low-lying single-particle states are predicted to be $[620]\frac{1}{2}^+$, $[624]\frac{7}{2}^+$ and $[622]\frac{3}{2}^+$. The strongly coupled band built on the $[734]\frac{9}{2}^-$ configuration would most probably result in M1-transitions carrying the dominant intensity. Other configurations, except $[622]\frac{3}{2}^+$, would reveal similar features.

The first attempt to study ^{253}No was performed with Gammasphere and FMA system via the ^{207}Pb(^{48}Ca,2n)^{253}No reaction [Kho 00]. The resulting recoil-gated γ-ray spectrum shows similar features to the spectrum obtained in the γ-ray study of ^{255}Lr discussed in the previous section. Only a few weak

γ-ray peaks were visible. The presence of intense No X-rays indicates that most of the yrast transitions proceed via internal conversion. For this reason, a conversion-electron study of this nucleus was performed with the collinear SACRED electron spectrometer at RITU.

In this experiment, a 500 $\mu g/cm^2$ thick highly enriched ($\approx$ 99 %) ^{207}Pb target was irradiated with 10 pnA ^{48}Ca beam for approximately 10 days. The beam energy was 219 MeV. The α-particle spectrum obtained from this reaction is shown in figure 4.13. In total, approximately 2000 correlated recoil-α-particle pairs were observed.

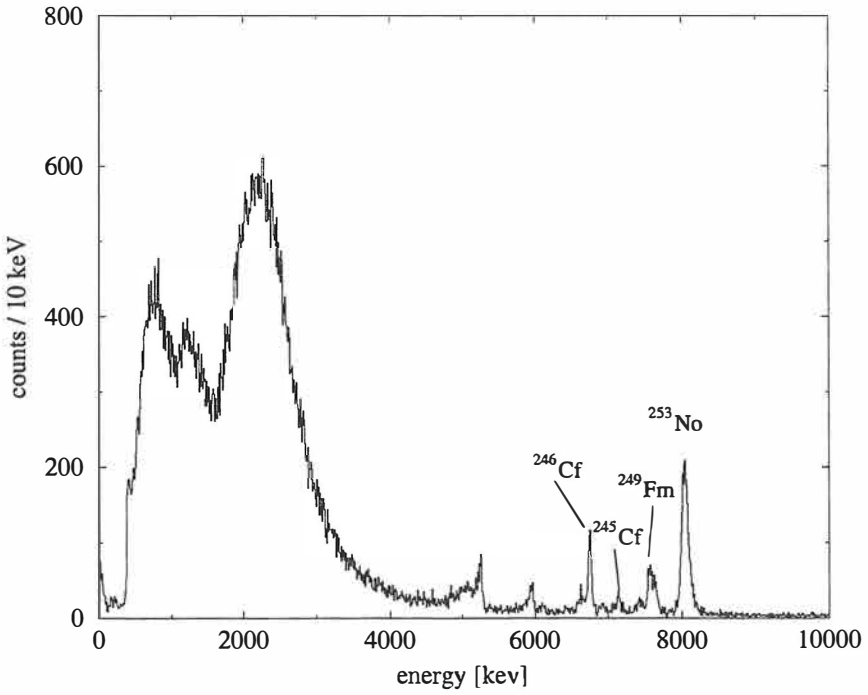

Figure 4.13 Total singles α-particle energy spectrum from the ^{48}Ca + ^{207}Pb reactions.

The recoil-gated and recoil-decay tagged conversion electron spectra, shown

in figure 4.14, clearly indicate a wide distribution of low-energy conversion electrons in the energy range 50 - 150 keV. In the recoil-gated spectrum, the shape of this distribution is relatively smooth so that identification of separate peaks is difficult. This is possibly due to the very closely separated peaks at this energy range. Due to the relatively poor resolution of the detector it is not possible to resolve candidate peaks from each other. The lack of electron lines above 150 keV indicates the presence of M1-transitions which mostly proceed via K-conversion above this energy. This is in accordance with the assignment of $[734]\frac{9}{2}^-$ for the ground state configuration.

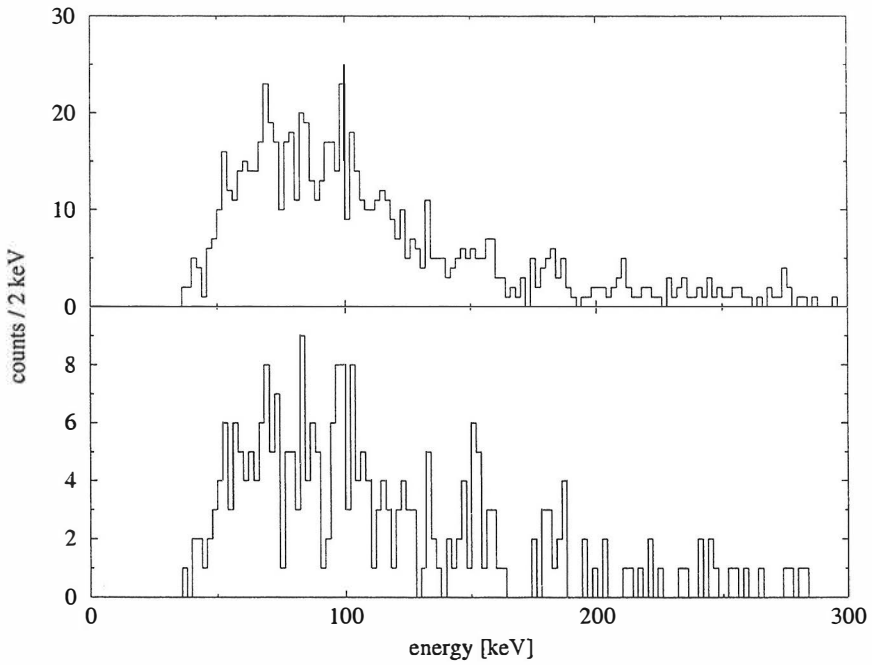

Figure 4.14 Recoil-gated (upper) and recoil-decay tagged (lower) electron spectra from ^{253}No.

4.3 Discussion

The energy of the 2^+ state is lower in ^{254}No than in ^{252}No. This is in accordance with the predictions that a local energy minimum for 2^+ states is at $N = 152$. According to the extrapolated energies of the 2^+ states in ^{252}No and ^{254}No, we can derive a value for the deformation parameter β_2 (see section 1.3) for these nuclei to be 0.25 ± 0.04 and 0.26 ± 0.04, respectively. These values are in good agreement with calculated values of approximately 0.25 [Pat 91].

The survival of ^{252}No and ^{254}No nuclei up to spin $\approx 20\hbar$ observed in the present work reveals that these nuclei survive against fission at least up to that spin. This state corresponds to an excitation energy of approximately 3 MeV. The regularity in the decrease of the γ-ray intensities shows no indication of the fission barrier causing a sudden band termination or strong deviations from the rotational pattern.

At low rotational frequencies the kinematic and dynamic moments of inertia for the ^{252}No and ^{254}No nuclei plotted in figure 4.15 show similar slowly increasing behaviour which may be due to the gradual alignment of quasiparticles. At the rotational frequency of approximately 200 keV, the ^{252}No nucleus seems to experience an upbend, possibly a result of the predicted neutron alignments. There is no indication of an upbend in ^{254}No.

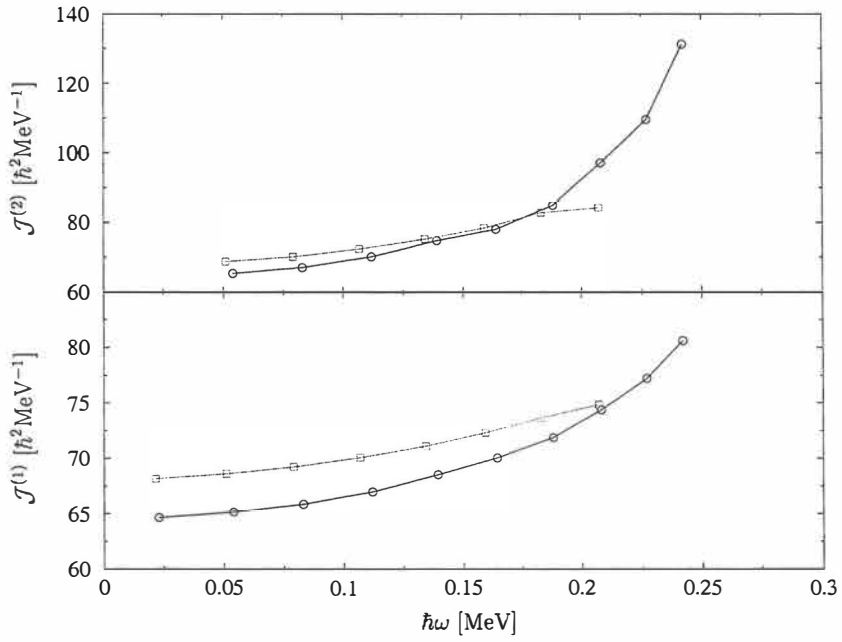

Figure 4.15 Kinematic $\mathcal{J}^{(1)}$ and dynamic $\mathcal{J}^{(2)}$ moments of inertia for ^{252}No (circles) and ^{254}No (squares) nuclei. An upbend can be seen in the curve for the ^{252}No nucleus at $\hbar\omega \approx 200$ keV.

Our conversion-electron spectroscopic study of ^{254}No clearly managed to show that the $4^+ \longrightarrow 2^+$ transition in this nucleus has an energy of approximately 102 keV as predicted by the VMI fit to the levels obtained in the γ-ray studies. The in-beam studies of odd-mass ^{253}No and ^{255}Lr indicate that most of the yrast transitions in these nuclei are highly converted M1-transitions. This suggests that for these nuclei the ground state configurations that result in M1-transitions carrying the dominant intensity are favoured. It is obvious that further electron-spectroscopic studies of these nuclei with improved energy resolution of the electron detector are needed. However, the interpretation of the obtained spectra will be difficult.

Chapter 5

Summary

Several target-area detector arrays were combined with the JYFL gas-filled recoil separator RITU. Recoil-gating and recoil-decay tagging techniques were utilised in in-beam studies of transfermium nuclei. The Jurosphere and SARI arrays were used for the γ-ray spectrosopic studies. The collinear SACRED conversion-electron spectrometer was designed and employed in these type of measurements for the first time. The power of this spectrometer was demonstrated in the observation of the $4^+ \longrightarrow 2^+$ transition in ^{254}No.

In this work, the ground state bands in ^{252}No and ^{254}No up to spin $16\hbar$ and $20\hbar$ were observed, respectively. The ground state deformation parameters β_2 were derived from the energies of the 2^+ states by using global systematics. On this basis we can conclude that these nuclei are deformed with a β_2-value of approximately 0.26. The result is in accordance with the prediction that the energy energy of the lowest 2^+ state has a local minimum at $N = 152$.

The in-beam γ-ray studies of odd-mass heavy elements ^{253}No and ^{255}Lr indicate that the de-excitations of the excited yrast states in these nuclei mainly proceed via a cascade of M1-transitions. For this reason, conversion-electron spectroscopic studies of these nuclei were clearly called for. The recoil-gated and recoil-decay tagged conversion-electron spectra obtained from ^{253}No also indicate the existence of cascades of yrast M1-transitions in this nucleus. However, the interpretation of the spectra obtained is difficult. The reason is

that very low-energy electrons (e.g. K-conversion of 150 - 200 keV transitions) cannot be detected.

More development is needed to improve the performance of the collinear SACRED conversion-electron spectrometer in in-beam measurements. The resolution of the detector needs to be improved in order to resolve the most prominent transitions. The background conditions can possibly be improved by using a set-up in a geometry where the beam is not passing through the HV-barrier, but this would require a larger deviation than 2.5° used in this spectrometer. This would increase the δ-electron background from the target. The detection efficiency at higher electron energies could be improved by applying a higher current through the solenoid coils. The mask of the detector could be redesigned in order to manufacture a detector that would balance the counting rate distribution over the detector area more than the detector used in this work. The design of the mask could be done on the basis of observed counting rates with the current detector.

The γ-ray study of ^{252}No shows that nuclei with production cross-sections on the order of 100 nb could be studied with the Ge-detector arrays used in this work. However, the in-beam studies of heavier elements which have a production cross-section at a level of approximately 10 nb are not accessible without several improvements. The background conditions in the γ-ray studies can be improved by using differential pumping at the target area. This would allow experiments to be performed without the carbon-foil separating the recoil-separator and beam-line volumes thus allowing experiments with higher beam intensity. The availability of a ^{50}Ti beam would allow us to study the structure of ^{256}Rf. This would require a more efficient γ-ray detector array with good Compton suppression and remarkably improved background conditions.

Appendix A

Relativistic corrections for electrons and gamma-rays

In-beam studies of nuclei involve the detection of particles and γ-rays emitted from a flying recoil. Typical recoil velocities are of the order of few % of the speed of light. This velocity is high enough to result in an observable energy shift (Doppler shift) for emitted particles and γ-rays detected in the laboratory frame with high-resolution detectors. The energy shift is also dependent on emission angle and due to the angular acceptance of the detector system, a broadening and peak-shape distortion of the peaks in the energy spectrum is observed. For this reason, relativistic corrections must be taken into account carefully. Doppler broadening needs to be considered when designing new types of detector arrays.

In order to calculate the energy shift, a transformation between two coordinate systems, the rest-frame of the recoil (x_i) and the laboratory frame (x_i'), are needed for four-momentum. In the special theory of relativity, this transformation is known as the Lorentz transformation. If the recoil is moving along the x_1-axis with a speed of v with respect to the laboratory frame, the Lorentz transformation for four-momentum can be written as (in the units c

$= 1$)

$$\begin{cases} p'_1 &= \gamma(p_1 + \beta E_{tot}) \\ p'_2 &= p_2 \\ p'_3 &= p_3 \\ p'_4 &= \gamma(E_{tot} + \beta p_1), \end{cases} \tag{A.1}$$

where $\beta = v/c$ and $\gamma = 1/\sqrt{1-\beta^2}$. In this notation E_{tot} is the full energy of the particle and it can be rewritten as $E_{tot} = E + m$, where E is the kinetic energy and m is the mass of the emitted particle. The scalar product $p_\mu p_\mu$ is invariant under Lorentz transformation, i.e.

$$p'_\mu p'_\mu = p_\mu p_\mu = p_1^2 + p_2^2 + p_3^2 - E_{tot}^2 = p^2 - E_{tot}^2 = -m^2,$$

a constant value for all inertial frames. When replacing E_{tot} with $E - m$ the invariance principle gives us a relationship between the momentum and the kinetic energy:

$$p^2 = E^2 + 2mE.$$

Furthermore, the invariance principle allows us to write the kinetic energy E' (shifted energy) as

$$E' = \sqrt{E_{tot}^2 + p'^2 - p^2} - m. \tag{A.2}$$

The frames can be aligned such that

$$\begin{cases} p_1 &= p\cos\theta \\ p_2 &= p\sin\theta \\ p_3 &= 0. \end{cases} \tag{A.3}$$

According to equation A.1, $p'_{2,3} = p_{2,3}$, and therefore we can simply write

$$p_1'^2 - p_1^2 = \frac{1}{1-\beta^2}\left(\beta^2 p_1^2 + 2p_1\beta(E+m) + \beta^2(E+m)^2\right).$$

By inserting this into equation A.2, and by using equation A.3, we finally get an equation for shifted energy E'

$$E' = \frac{E + m + \beta\cos\theta\sqrt{E^2 + 2mE}}{\sqrt{1-\beta^2}} - m. \tag{A.4}$$

In the laboratory frame, we observe E' at an angle of θ' and therefore we need an equation to calculate the unshifted energy E. This can be derived from equation A.4 in a simple manner by replacing unprimed quantities E, β and θ with primed quantities (measured values) E', $\beta' = -\beta$ and θ'

$$E = \frac{E' + m - \beta \cos\theta' \sqrt{E'^2 + 2mE'}}{\sqrt{1-\beta^2}} - m. \tag{A.5}$$

Energy shifts for electrons in the energy range 0 - 500 keV with different β-values are plotted in figure A.1. In this figure, it has been assumed that θ' = 160°, which is a relatively good approximation for the collinear SACRED spectrometer. The Lorenz invariance $p_\mu p_\mu$ for γ-rays is $p_\mu p_\mu = 0$ which leads to the well known Doppler correction formula for γ-rays (by inserting m = 0 in equation A.5)

$$E = \frac{E'(1 - \beta \cos\theta')}{\sqrt{1-\beta^2}} \ . \tag{A.6}$$

For small β values, this can be approximated to $E \approx E'(1 - \beta \cos\theta')$. The relative energy shift for γ-rays is not dependent on the energy, whereas for electrons this is clearly not true.

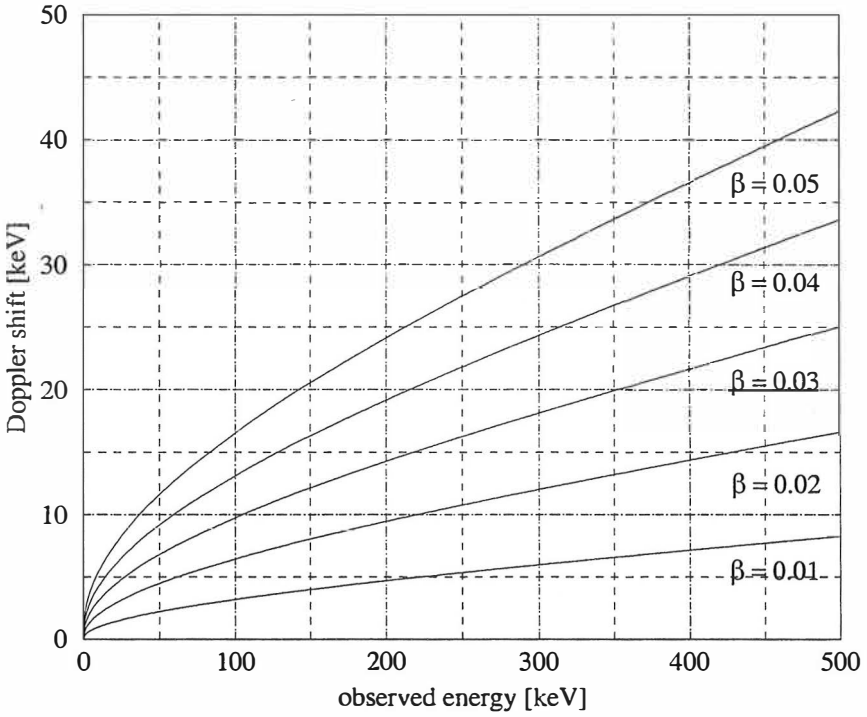

Figure A.1 Energy shift for electrons detected in the laboratory frame at an angle of $\theta' = 160°$.

Bibliography

[Ako 98] Y.A. Akovali, Nucl. Data Sheets 84 (1998) 1.

[Bac 78] H. Backe, L. Richter, R. Willwater, E. Kankeleit, E. Kuphal, B. Martin and Y. Nakayama, Z. Phys. A 285 (1978) 159.

[Bea 92] C.W. Beausang, S.A. Forbes, P. Fallon, P.J. Nolan, P.J. Twin, J.N. Mo, J.C. Lisle, M.A. Bentley, J. Simpson, F.A. Beck, D. Curien, G. deFrance, G. Duchêne and D. Popescu, Nucl. Instr. and Meth. A 313 (1992) 37.

[Boh 75] A. Bohr and B.R. Mottelson, Nuclear Structure Volume II: Nuclear Deformations, W.A. Benjamin Inc., New York (1975).

[But 96a] P.A. Butler, P.M. Jones, K.J. Cann, J.F.C. Cocks, G.D. Jones, R. Julin and W.H. Trzaska, Nucl. Instr. and Meth. A 381 (1996) 433.

[But 96b] P.A. Butler and W. Nazarewicz, Rev. Mod. Phys., vol. 68 No. 2 (1996) 349.

[But 01] P.A. Butler, A.J. Chewter, H. Kankaanpää, R.-D. Herzberg, F. Becker, J.F.C. Cocks, O. Dorvaux, K. Eskola, J. Gerl, P.T. Greenlees, N. Hammond, K. Helariutta, F.P. Heßberger, M. Houry, R.D. Humphreys, A. Hürstel, G.D. Jones, P.M. Jones, R. Julin, S. Juutinen, A. Keenan, H. Kettunen, T.L. Khoo, W. Korten, P. Kuusiniemi, Y. Le Coz, M. Leino, R. Lucas, M. Muikku, P. Nieminen, R.D. Page, T. Page, P. Rahkila, P. Reiter, A. Savelius, Ch. Schlegel, C. Theisen, W.H. Trzaska, J. Uusitalo and H.J. Wollersheim, Acta Phys. Polonica B 32 (2001) 619.

[Cre 91] J. Cresswell, Eurogam project documentation, EDOC073, Nuclear structure Software Support Group, Liverpool University, February 1991

[Ćwi 94] S. Ćwiok, S. Hofmann and W. Nazarewicz, Nucl. Phys. A 573 (1994) 356.

[Ćwi 00] S. Ćwiok, Private communications, communicated by P.A. Butler.

[Dav 89] C.N. Davids and J.D. Larson, Nucl. Instr. and Meth. B 40/41 (1989) 1224.

[Enq 96] T. Enqvist, Ph.D. Thesis, Department of Physics, University of Jyväskylä, Research Report No. 3/1996.

[Fle 76] G.N. Flerow, Yu. Ts. Oganessian, A.A. Pleve, N.V. Pronin and Yv. P. Tretyakov, Nucl. Phys. A 267 (1976) 359.

[Ghi 67] A. Ghiorso, T. Sikkeland and M.J. Nurmia, Phys. Rev. Lett. 18 (1967) 401.

[Gre 01] P.T. Greenlees, H. Kankaanpää et al., to be published.

[Gro 62] L. Grodzins, Phys. Lett. 2 (1962) 88.

[Har 65] S.M. Harris, Phys. Rev. B 138 (1965) 509.

[Hei 95] P. Heikkinen and E. Liukkonen, 14^{th} International Conference on Cyclotrons and Their Applications, Cape Town, October 8 - 13 (1995).

[Hel 99] K. Helariutta, J.F.C. Cocks, T. Enqvist, P.T. Greenlees, P. Jones, R. Julin, S. Juutinen, P. Jämsen, H. Kankaanpää, H. Kettunen, P. Kuusiniemi, M. Leino, M. Muikku, M. Piiparinen, P. Rahkila, A. Savelius, W.H. Trzaska, S. Törmänen, J. Uusitalo, R.G. Allatt, P.A. Butler, R.D. Page and M. Kapusta, Eur. Phys. J. A 6 (1999) 289.

[Her 01a] R.-D. Herzberg, H. Kankaanpää, P.A. Butler, N. Amzal, A.J. Chewter, N. Hammond, G.D. Jones, R.D. Page, C. Scholey, O. Stezowski, M. Leino, R. Julin, J.F.C. Cocks, O. Dorvaux, P.T. Greenlees, K. Helariutta, P.M. Jones, S. Juutinen, H. Kettunen, P. Kuusiniemi, M. Muikku, P. Nieminen, P. Rahkila, W.H. Trzaska, J. Uusitalo, F.P. Heßberger, J. Gerl, Ch. Schlegel, H.J. Wollersheim, W. Korten, F. Becker, Y. Le Coz, K. Hauschild, M. Houry, R. Lucas, Ch. Theisen, P. Reiter, T.L. Khoo, C.J. Lister and K. Eskola, to be published.

[Her 01b] R.-D. Herzberg, H. Kankaanpää et al., to be published.

[Heß 85] F.P. Heßberger, GSI Report GSI-85-11 (1985).

[Heß 89] F.P. Heßberger, S. Hofmann, G. Münzenberg, K.-H. Schmidt, P. Armbruste and R. Hingmann, Nucl. Instr. and Meth. A 274 (1989) 522.

[Heß 97] F.P. Heßberger, S. Hofmann, V. Ninov, P. Armbruster, H. Folger, G. Münzenberg, H.J. Schött, A.G. Popeko, A.V. Yeremin, A.N. Anreyev and S. Saro, Z. Phys. A 359 (1997) 415.

[Hof 99] S. Hofmann, Physics World, March 1999 p19.

[Jen 00] D.G. Jenkins, M. Muikku, P.T. Greenlees, K. Hauschild, K. Helariutta, P.M. Jones, R. Julin, S. Juutinen, H. Kankaanpää, N.S. Kelsall, H. Kettunen, P. Kuusiniemi, M. Leino, C.J. Moore, P. Nieminen, C.D. O'Leary, R.D. Page, P. Rahkila, W. Reviol, M.J. Taylor, J. Uusitalo and R. Wadsworth, Phys. Rev. C 62 (2000) 021302(R).

[Jon 99] P. Jones, P. Rahkila, J.F.C. Cocks, K. Helariutta, R. Julin, S. Juutinen, H. Kankaanpää, H. Kettunen, P. Kuusiniemi, Y. Le Coz, M. Leino, M. Muikku, P. Nieminen and A. Savelius, Acta Phys. Polonica B 30 (1999) 671.

[Kan 01] H. Kankaanpää, P.A. Butler, P.T. Greenlees, R-D. Herzberg, R.D. Humphreys, G.D. Jones, P. Jones, R. Julin, A. Keenan, L. Miettinen, P. Rahkila and C. Scholey, to be published in Nucl. Instr. and Meth.

[Ket 01] H. Kettunen, P.T. Greenlees, K. Helariutta, P. Jones, R. Julin, S. Juutinen, P. Kuusiniemi, M. Leino, M. Muikku, P. Nieminen and J. Uusitalo, Acta. Phys. Polonica B 32 (2001) 989.

[Kho 00] T.L. Khoo, Private communication.

[Kra 88] K.S. Krane, Introductory Nuclear Physics, John Wiley and Sons, New York (1988).

[LeC 99] Y. Le Coz, F. Becker, H. Kankaanpää, W.Korten, E. Mergel, P.A. Butler, J.F.C. Cocks, O. Dorvaux, D. Hawcroft, K. Helariutta, R.-D. Herzberg, M. Houry, H. Hübel, P. Jones, R. Julin, S. Juutinen, H. Kettunen, P. Kuusiniemi, M. Leino, R. Lucas, M. Muikku, P. Nieminen, P. Rahkila, D. Rossbach, A. Savelius and Ch. Theisen, EPJ direct A (1999) 1.

[Lei 81] M.E. Leino, S. Yashita and A. Ghiorso, Phys. Rev. C 24 (1981) 2370.

[Lei 95] M. Leino, J. Äystö, T. Enqvist, P. Heikkinen, A. Jokinen, M. Nurmia, A. Ostrowski, W.H. Trzaska, J. Uusitalo, K. Eskola, P. Armbruster and V. Ninov, Nucl. Instr. and Meth. B 99 (1995) 653.

[Lei 99] M. Leino, H. Kankaanpää, R.-D. Herzberg, A.J. Chewter, F.P. Heßberger, Y. Le Coz, F. Becker, P.A. Butler, J.F.C. Cocks, O. Dorvaux, K. Eskola, J. Gerl, P.T. Greenlees, K. Helariutta, M. Houry, G.D. Jones, P. Jones, R. Julin, S. Juutinen, H. Kettunen, T.L. Khoo, A. Kleinböhl, W. Korten, P. Kuusiniemi, R. Lucas, M. Muikku, P. Nieminen, R.D. Page, P. Rahkila, P. Reiter, A. Savelius, Ch. Schlegel, Ch. Theisen, W.H. Trzaska and H.-J. Wollersheim, Eur. Phys. J. A 6 (1999) 63.

[Mos 89] M. Moszyński, J.H. Bjerregard, J.J. Gaardhøje, B. Herskind, P. Knudsen, G. Sletten, Nucl. Instr. and Meth. A 280 (1989) 73.

[Mui 00] M. Muikku, Ph.D. Thesis, Department of Physics, University of Jyväskylä, Research Report No. 7/2000.

[Mun 99] I. Muntian, Z. Patyk, A. Sobiczewski, Phys. Rev. C60 (1999) 041302.

[Mün 81] G. Münzenberg, W. Faust, F.P. Heßberger, S. Hofmann, W. Reisdorf, K.-H. Schmidt, W.F.W. Schneider, H. Schött, P. Armbruster, K. Güttner, B. Thuma, H. Ewald and D. Vermeulen, Nucl. Instr. and Meth. A 186 (1981) 423.

[Mün 85] G. Münzenberg, S. Hofmann, H. Folger, F.P. Heßberger, J. Keller, K. Poppensieker, B. Quint, W. Reisdorf, K.-H. Schmidt, H.J. Schött, P. Armbruster, M.E. Leino and R. Hingmann, Z. Phys. A 322 (1985) 227.

[Möl 95] P. Möller, J.R. Nix, W.D. Myers and W.J. Swiatecki, At. Data Nucl. Data Tables 59 (1995) 185.

[Nil 55] S.G. Nilsson, Kgl. Dan. Viden. Selsk. Mat. Fys. Medd. 29 No.16 (1955) 1.

[Nol 85] P. Nolan, D.W. Gifford and P.J. Twin, Nucl. Instr. and Meth. A 236 (1985) 95.

[Pau 95] E.S. Paul, P.J. Woods, T. Davidson, R.D. Page, P.J. Sellin, C.W. Beausang, R.M. Clark, R.A. Cunningham, S.A. Forbes, D.B. Fossan, A. Gizon, J. Gizon, K. Hauschild, I.M. Hibbert, A.N. James, D.R. LaFosse, I. Lazarus, H. Schnare, J. Simpson, R. Wadsworth and M.P. Waring, Phys. Rev. C 51 (1995) 78.

[Pat 91] Z. Patyk and A. Sobiczewski, Nucl. Phys. A 533 (1991) 132.

[Rei 99] P. Reiter, T.L. Khoo, C.J. Lister, D. Seweryniak, I. Ahmad, M. Alcorta, M.P. Carpenter, J.A. Cizewski, C.N. Davids, G. Gervais, J.P. Greene, W.F. Henning, R.V.F. Janssens, T. Lauritsen, S. Siem, A.A. Sonzogni, D. Sullivan, J. Uusitalo, I. Wiedenhöver, N. Amzal, P.A. Butler, A.J. Chewter, K.Y. Ding, N. Fotiades, J.D. Fox, P.T. Greenlees, R.-D. Herzberg, G.D. Jones, W. Korten, M. Leino and K. Vetter, Phys. Rev. Lett. 82 (1999) 509.

[Rei 00] P. Reiter, T.L. Khoo, T. Lauritsen, C.J. Lister, D. Seweryniak, A.A. Sonzogni, I. Ahmad, N. Amzal, P. Bhattacharyya, P.A. Butler, M.P. Carpenter, A.J. Chewter, J.A. Cizewski, C.N. Davids, K.Y. Ding, N. Fotiades, J.P. Greene, P.T. Greenlees, A. Heinz, W.F. Henning, R.-D. Herzberg, R.V.F. Janssens, G.D. Jones, H. Kankaanpää, F.G. Kondev, W. Korten, M. Leino, S. Siem, J. Uusitalo, K. Vetter and I. Wiedenhöver, Phys. Rev. Lett. 84 (2000) 3542.

[Ros 78] F. Rosel, H.M. Fries, K. Alder, and H.C. Pauli , Atomic and Nuclear Data Tables, vol 21 (1978).

[Sch 89] M.R. Schmorak, Nucl. Data Sheets 57 (1989) 515.

[She 99] S.L. Shepherd, P.J. Nolan, D.M. Cullen, D.E. Appelbe, J. Simpson, J. Gerl, M. Kaspar, A. Kleinböhl, I. Peter, M. Rejmund, H. Schaffner, C. Schlegel and G. deFrance, Nucl. Instr. and Meth. A 434 (1999) 373.

[Sim 86] R.S. Simon, K.-H. Schmidt, F.P. Heßberger, S. Hlavac, M. Honusek, G. Münzenberg, H.-G. Clerc, U. Gollerthan and W. Schwab, Z. Phys. A 325 (1986) 197.

[Ste 72] F.S. Stephens, R.M. Diamond, J.R. Leigh, T. Kammuri and K. Nakai, Phys. Rev. Lett. 29 (1972) 438.

[Swi 82] W.J. Swiatecki, Nucl. Phys. A 376 (1982) 275.

[Trz 90] W.H. Trzaska, Nucl. Instr. and Meth. A 297 (1990) 223.

[Tür 88] A. Türler, H.W. Gäggeler, D.T. Jost, P. Armbruster, W. Brüchle, H. Folger, F.P. Heßberger, S. Hofmann, G. Münzenberg, V. Ninov, M. Schädel, K. Sümmerer, J.V. Kratz and U. Scherer, Z. Phys. A 331 (1988) 363.

[Uus 96] J. Uusitalo, Ph.D. Thesis, Department of Physics, University of Jyväskylä, Research Report No. 4/1996.

[Wei 35] C.F. von Weizsäcker, Z. Phys. 96 (1935) 431.